minerals

MDPI

Article

Low Temperature Serpentinite Replacement by Carbonates during Seawater Influx in the Newfoundland Margin

Suzanne Picazo [1], Benjamin Malvoisin [1,2,*], Lukas Baumgartner [1] and Anne-Sophie Bouvier [1]

[1] Institut des Sciences de la Terre, University of Lausanne, Quartier UNIL-Mouline Bâtiment Géopolis, CH-1015 Lausanne, Switzerland; suzanne.picazo@gmail.com (S.P.); lukas.baumgartner@unil.ch (L.B.); anne-sophie.bouvier@unil.ch (A.-S.B.)

[2] University Grenoble Alpes, University Savoie Mont Blanc, CNRS, IRD, IFSTTAR, ISTerre, 38000 Grenoble, France

* Correspondence: benjamin.malvoisin@univ-grenoble-alpes.fr; Tel.: +33-476-514-072

Received: 22 January 2020; Accepted: 11 February 2020; Published: 18 February 2020

Abstract: Serpentinite replacement by carbonates in the seafloor is one of the main carbonation processes in nature providing insights into the mechanisms of CO_2 sequestration; however, the onset of this process and the conditions for the reaction to occur are not yet fully understood. Preserved serpentine rim with pseudomorphs of carbonate after serpentine and lobate-shaped carbonate grains are key structural features for replacement of serpentinite by carbonates. Cathodoluminescence microscopy reveals that Ca-rich carbonate precipitation in serpentinite is associated with a sequential assimilation of Mn. Homogeneous $\delta^{18}O$ values at the µm-scale within grains and host sample indicate low formation temperature (<20 °C) from carbonation initiation, with a high fluid to rock ratio. $\delta^{13}C$ (1–3 ± 1‰) sit within the measured values for hydrothermal systems (−3–3‰), with no systematic correlation with the Mn content. $\delta^{13}C$ values reflect the inorganic carbon dominance and the seawater source of CO_2 for carbonate. Thermodynamic modeling of fluid/rock interaction during seawater transport in serpentine predicts Ca-rich carbonate production, at the expense of serpentine, only at temperatures below 50 °C during seawater influx. Mg-rich carbonates can also be produced when using a model of fluid discharge, but at significantly higher temperatures (150 °C). This has major implications for the setting of carbonation in present-day and in fossil margins.

Keywords: carbonation; CO_2 sequestration; replacement process; low temperature carbonate precipitation; Secondary Ion Mass Spectrometer; seawater influx; hydrothermal circulation; ophicalcite

1. Introduction

Carbonation of peridotites occurs along rifted margins (e.g., the Western Iberia margin, [1] and references therein) and at Mid-Ocean Ridges (MORs; e.g., [2,3]). It is also commonly observed in ophiolites in the Alpine Tethys (e.g., [4]), the Pyrenees ([5] and references therein), Norway (e.g., [6]), Oman (e.g., [7]) and Québec [8]. Carbonated peridotites include ophicarbonates commonly associated to brecciated peridotites, cemented by carbonate, and created by tectonic, hydrothermal and/or sedimentary processes [9,10]. Metasomatic processes responsible for pervasive replacement of serpentine by calcite occur at slow-spreading ridges and in magma-poor passive margins, where peridotites are exposed on the seafloor during tectonic extension [11,12] and has been described in fossil margins (Chenaillet in the Alpine Tethys; [13]). Understanding carbonation in natural systems provides constraints to develop efficient engineering strategies for atmospheric CO_2 sequestration [14,15].

The heat released during magma cooling triggers seawater circulation in the upper part of the lithosphere. During hydrothermal circulation, mantle rocks are progressively replaced by hydrous minerals including serpentine and brucite [16,17]. This serpentinization reaction is also a redox reaction in which the ferrous iron contained in peridotite is oxidized to form magnetite and ferric serpentine, whereas water is reduced to form hydrogen [18]. Recent studies on the venting temperature of hydrothermal fluids from the Lucky Strike hydrothermal system emphasize that hydrothermal fluid circulation is subdivided into major (km-scale) and minor (m-scale) convection cells; the major cells lead to focused venting of high temperatures at the outflow, whereas the minor convection cells show mixing with seawater (4 °C) at the meter-scale leading to venting of diffuse fluids at low temperatures [19,20]. The composition of the fluid formed during fluid-peridotite interaction is expected to evolve from seawater to a high pH (9–11), hydrogen- and methane-rich fluid [18]. Highly alkaline fluids are expelled at low temperature (40–75 °C, [21,22]) at the Lost City Hydrothermal Field (LCHF). Such fluids promote Ca-carbonate precipitation ± brucite in chimneys and in veins [23,24]. Similar mineralogy has been observed within the Iberian margin, where the mixing zone provides an environment favoring microbial development (Ocean Drilling Program (ODP) Leg 149 Site 897; [25]). Peridotite-hosted hydrothermal systems exist at MORs such as the Mid-Atlantic Ridge (MAR; Kane Fracture Zone [26]; 15° N [27]) and in passive margins (e.g., Western Iberia margin; [25]). Fossil systems are also found in mountain belts like the Piemonte-Liguria ophiolites (e.g., Chenaillet, [28]). Acidic (pH ~3) and high-temperature (>300 °C) fluids were also sampled at other peridotite-hosted hydrothermal systems such as Rainbow and Logatchev, suggesting a contribution of mafic bodies [18]. Ultimately, fluid-rock interactions in the presence of mafic rocks may lead to crystallization of Si-rich phases, like talc [10,29] or quartz [30].

The composition of carbonates found in ophicarbonates varies between Mg and Ca-rich end-members. Calcite, aragonite, magnesite and dolomite show variable isotopic signatures, with $\delta^{18}O_{VSMOW}$ ranging from 8.3‰ to 36.6‰ and $\delta^{13}C_{VPDB}$ from −4.5‰ to 4.5‰ (see Supplementary Table S1). As a result, temperatures of carbonate crystallization estimated using $\delta^{18}O$ range from 1 up to ~200 °C [26,27], assuming seawater isotopic compositions for the fluid. This can be used to suggest precipitation under completely different conditions [27] from seawater on the seafloor [3] to high temperature hydrothermal fluids (100–150 °C; [13]). However, details about the different conditions are not well constrained nor how it relates to the process of carbonate formation. In hydrothermal systems, carbonates may be formed during either seawater influx or hydrothermal fluid discharge, involving different temperatures, compositions and fluid flow regimes.

Here, we investigate the process of serpentinite replacement by carbonates in a sample from the Newfoundland (NF) margin. In order to constrain the timing of calcite replacement, we first establish the brecciation event succession. Then we characterize the textures of calcite growth and their in-situ oxygen isotopic signature from core to rim. We couple our micro-textural observations and O and C isotopic measurements with a thermodynamic model to provide new constraints on the conditions of carbonation in mantle rocks exposed on the seafloor. Furthermore, we compile published O–C data from present-day and fossil distal margins and slow-spreading ridge ophicarbonates to discuss the possible re-equilibration of O–C in ophicarbonates during metamorphism.

2. Geological Setting

In the Newfoundland hyper-extended margin and conjugate Iberian margin, subcontinental lithospheric mantle was exhumed on the seafloor by detachment faulting. During the mantle exposure on the seafloor, a superposition of near-seafloor processes i.e., tectonic, hydrothermal and sedimentary brecciation occurred, resulting in tectono-sedimentary breccias [31–33]. Ophicarbonates are observed from the proximal to the distal margin of both the Newfoundland and Iberian margins. Carbonation processes overlap the brecciation, leading to calcite veins, replacement of serpentine and carbonate cement. The tectono-sedimentary breccias rework exhumed serpentinized footwall and thus preserved every stage of carbonation from its onset. Previous work from the Iberian margin has estimated that

the temperature of carbonation in calcite veins and cement was < 45 °C based on $\delta^{18}O_{VSMOW}$ values of 25‰ to 35‰ [1,3,34–36]. The carbonation was thus interpreted as a near-surface cold process [35].

Here, we study samples from the International Ocean Discovery Program (IODP) site 1277 (Figure 1; [37]). The drill core contains serpentinized peridotites and locally magmatic intrusions (e.g., alkaline sills of 124–112 Ma, followed by Mid-Ocean Ridge Basalt-type magmatism <112 Ma at the onset of oceanic spreading, [38,39] and references therein). The drill core is also composed of brecciated serpentinized peridotites over 20 m (Figure 1c); we focus on these serpentinite samples that show evidence of replacement by carbonates.

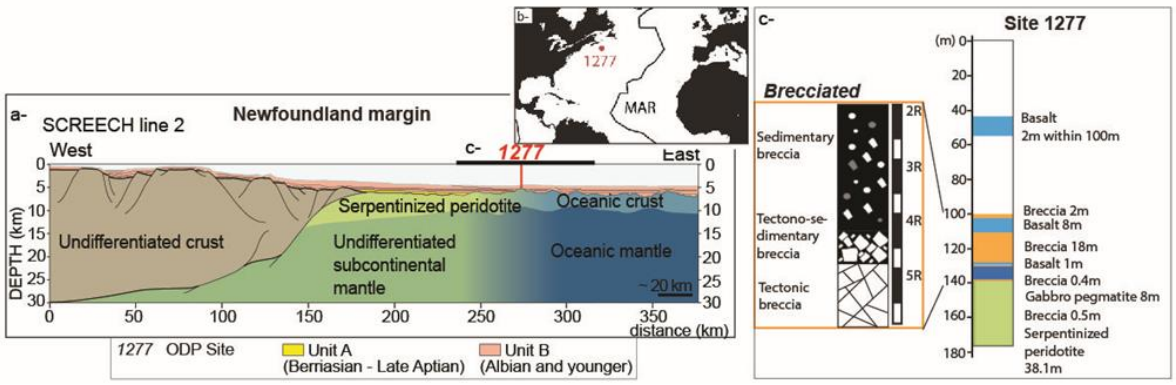

Figure 1. (**a**) Interpretative cross-section after Sutra and Manatschal [40] based on the seismic lines Lusigal 12 and of the TGS-NOPEC Geophysical Company for Iberia margin, and line 2 of the Study of Continental Rifting and Extension on the Eastern Canadian Shelf (SCREECH) project for Newfoundland. (**b**) Location of the Site 1277 in the Mid-Atlantic Ridge (MAR). (**c**) Sketch of the repartition of drilled mineralogies.

3. Methods

3.1. Microscopy

Scanning Electron Microscopy images were acquired using a Tescan Mira LMU FE-SEM (ISTe, University of Lausanne (UniL), Lausanne, Switzerland) operated at an acceleration voltage of 20 kV and a probe current of 20 nA. We used cold cathodoluminescence (CL) microscopy (model 8200 MkII (OPEA^{TM}), ISTe, UniL, Lausanne, Switzerland) to qualitatively estimate the variation in Mn content [41]. Light orange corresponds to a high Mn concentration whereas dark red is associated with low Mn concentrations. Electron microprobe analyses were conducted on a JEOL JKA-8530F (UniL, Lausanne, Switzerland), under beam of 15 nA and current of 10 nA as proposed by Lane and Dalton [42].

3.2. Secondary Ion Mass Spectrometer (SIMS) Analyses of Calcite

We measured carbonate grains in the core of the serpentine mesh textures using a Secondary Ion Mass Spectrometer Cameca 1280HR. We used a 10 kV Cs^+ primary beam, a ~1.5 nA current, resulting in a ~15 µm beam size. The electron flood gun, with normal incidence, was used to compensate charges.

For oxygen isotope measurements, ^{16}O and ^{18}O were analyzed with a mass resolving power of 2400 and collected in 2 faraday cups (10^{10} and 10^{11} Ω) in multi-collection mode. Each analysis takes ~4 min, including pre-sputtering (30 s) and automated centering of secondary electrons. This setting allowed an average reproducibility of ±0.28‰ (2 standard deviations (2 SD)) on an in house calcite reference material (UNIL_C1; $\delta\ ^{18}O_{VSMOW}$ = 18.29 ± 0.12‰ (2 standard error (2 SE))) at the beginning of each session. A set of 4 analyses of the calcite standard were also measured every 12 analyses for monitoring the instrument stability. The variation of the calcite standard over the 24 h session was ±0.52‰ (2 SD), suggesting a magnetic drift, for which the data were corrected. The error reported for samples reflected the 2 SD bracket between the surrounding set of standard analyses.

^{12}C and ^{13}C, measured in a second SIMS session, were separated using a mass resolving power of 4600, and collected in 2 faraday cups (both 10^{11} Ω). Each analysis takes ~4–6 min, including pre-sputtering (45 s) and automated centering of secondary electrons. This setting allowed an average reproducibility of ±0.6‰ (2 SD) on a calcite in house standard (UNIL_C1; $\delta\ ^{13}C_{VPDB}$ = 0.64 ± 0.08‰ (2 SE)) at the beginning of the session. A set of 4 analyses of a calcite standard was also measured every 10 unknowns; the variation of the calcite standard over the entire session (~3 h) was ±0.8‰ (2 SD), suggesting a slight magnetic drift. The error reported for samples reflected the 2 SD bracket between the surrounding set of standard analyses.

During both sessions, the faraday cups were calibrated at the beginning of the sessions using a calibration routine. Mass calibrations were performed at the beginning of the sessions and again after 12 h for the ^{18}O session.

We converted the measured $\delta^{18}O_{VSMOW}$ values from calcite into temperatures using the standard procedure of Kim and O'Neil [43] and assumed that calcite crystallized in equilibrium with seawater with a $\delta^{18}O_{VSMOW}$ = 0‰ at present-day, and a $\delta^{18}O_{VSMOW}$ = −1.2‰ for an ice-free world [44].

3.3. Thermodynamic Modeling

Fluid/rock interaction was modelled at the equilibrium with the EQ3/6 software [45]. The evolution of the mineralogy and the fluid chemistry were predicted for oceanic serpentinized peridotite during hydrothermal fluid recharge or discharge. We model hydrothermal circulation in one dimension with a medium discretized in a sequence of 50 to 60 boxes. The temperature was fixed in each box and either linearly increases (recharge) or decreases (discharge) from one box to the other along the flow path (Figure 2). The simulations consisted of 3000 to 7000 iterations subdivided into two steps. First, the composition of the fluid phase in equilibrium with the solid was calculated independently in each box. This induces mass transfer between the solid and the fluid. The aim of this model was to determine the impact on mineralogical composition of fluid-mediated mass transfer from low to high temperatures (recharge) or high to low temperatures (discharge). Therefore, during the second step, the fluid of modified composition was transferred from one box to the next one in flow direction, while seawater with fixed composition was introduced into the first box (Figure 2). This latter step conserves mass. Time is not a parameter of the model since time dependent processes such as fluid flow, diffusion or reaction kinetics were not considered. To determine the extent of fluid-rock interaction, we used the cumulative mass of fluid introduced in the first box of the model ($(W/R)_d$; scaled to 1 kg of solid initially present in this box). This parameter could seem similar to the water to rock ratio commonly used in thermodynamic calculations (e.g., [46]), but it does not correspond to a single calculation at the equilibrium since over the number of iterations it integrates the amount of fluid added in the first box (it is thus a "dynamic" water to rock ratio). This water to rock ratio should ideally be of 2×10^{-2} to correspond to the porosity of ~ 5% measured in serpentinized peridotites [47]. However, with such a low amount of fluid, the computing time is too long to obtain significant mass transfer leading to carbonates formation. Therefore, at each iteration, we added into the model 38 kg (discharge) or 380 kg (recharge) of fluid (for 1 kg of solid) in the first box. Thermodynamic calculations at the equilibrium were performed with the database of Johnson et al. [48] with additional data for ferrous and ferric serpentine and ferrous brucite from Klein et al. [49] (see [50] for details). No organic components were considered. In the calculations, we suppressed the reduction of carbon by H_2 to account for the slow kinetics of methanogenesis reactions [51]. The composition of the reacting serpentine was initially fixed at $Mg_{2.77}Fe^{2+}_{0.13}Fe^{3+}_{0.13}Si_{1.94}O_5(OH)_4$ based on microprobe analyses. Serpentine composition can then evolve as a result of fluid-rock interactions. Iron oxidation state in serpentine was not determined, therefore, half of the iron was assumed to be trivalent, based on the compilation of serpentine composition by Evans [52], in agreement with the thermodynamic calculations by Klein et al. [48] and the μ-X-ray Absorption Near Edge Structure serpentine analyses on mesh textures by Andreani et al. [53]. The composition of seawater introduced in the first box of the model is given in Table S3. Simulations were run at a constant pressure of 50 MPa for simplicity.

This pressure corresponds to the lithostatic pressure expected at drill site 1277, where drilling was performed at 4600 m water-depth up to 180 m below the seafloor. As expected, tests of the respective impacts of temperature and pressure on the thermodynamic equilibrium show that temperature is the primary control of the stable assemblage whereas pressure variations are less important in the pressure and temperature ranges relevant to MORs (4 to 350 °C and 20 to 50 MPa).

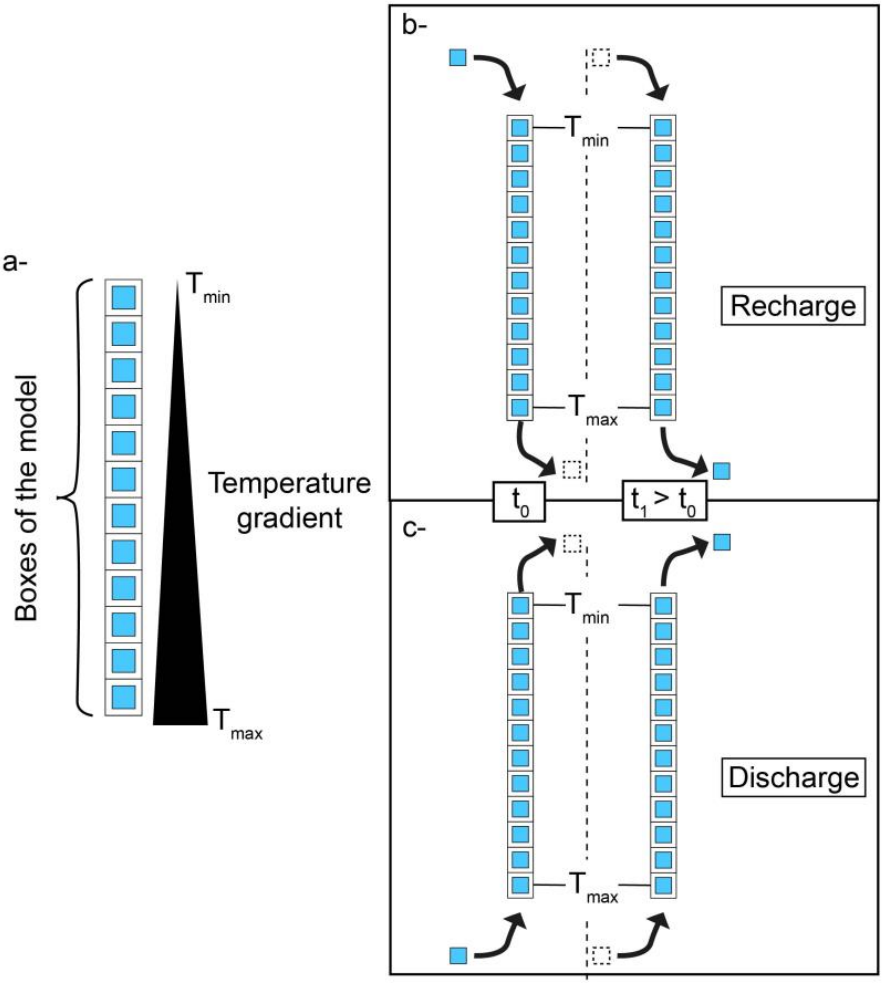

Figure 2. Sketch summarizing the modeling approach. (**a**) The model consists in calculating the equilibrium of a fluid + solid system in a series of boxes in which the fluid is transferred from one box to the next one at each time step. Two flow directions were investigated, either flow from high to low temperatures (discharge model) or from low to high temperatures (recharge model). Seawater was introduced in the first box of the model at 250 °C in the discharge model (**b**) and at 4 °C in the recharge model (**c**).

We applied equilibrium thermodynamics at low temperature in far from the equilibrium conditions. Reaction kinetics may prevent the achievement of equilibrium in these conditions. Taking into account reaction kinetics is fraught with uncertainty due to the lack of data on reaction rates in hydrothermal conditions and the need for modeling other time-dependent processes such as fluid flow. Several studies investigated the coupling between reaction kinetics and fluid flow in hydrothermal systems [54–56], but they simplified the system to a single chemical reaction and are therefore not able to model the changes in chemical composition investigated here. We therefore chose to calculate the system composition at the equilibrium towards which the system tends [57]. Such calculations were successfully applied to processes occurring at MORs (e.g., [47,48]). The use of equilibrium thermodynamics may be

challenged by the production of metastable phases during reaction. The main minerals formed here are serpentine and carbonates. Metastable serpentine minerals such as chrysotile have similar composition and thermodynamic properties to stable phases (lizardite; [58]). They will thus have a limited effect on the model outputs. However, Mg-carbonates (i.e., magnesite and dolomite) have precipitation kinetics at least 6 orders of magnitude slower than calcite precipitation at ambient conditions [59]. The high activation energy of Mg-carbonate precipitation makes Mg-carbonates formation possible at high temperature. Because of the slow Mg-carbonate kinetic reaction, we run both simulations including and excluding Mg-carbonate precipitation. Finally, we assumed thermodynamic equilibrium in each box of the model. This requires that transport processes (i.e., diffusion and advection) are fast enough compared to the reaction to achieve equilibrium at a scale of several meters.

4. Results

4.1. Brecciation and Carbonate Crystallization

The 20 m-thick layer of tectono-sedimentary breccias drilled at Site 1277 (Figure 1; [37]) contains several calcite generations recognized by their crosscutting relationship and angular to rounded clasts of serpentinite (Figure 3). The calcite occurs in three contexts: it precipitates in veins crosscutting the clasts and formed during tectonic brecciation (type 1; Figure 4a,b); it constitutes the sedimentary component of the breccia cement (type 2; Figures 4b and 5b) and it crystallizes in the core of the serpentinite clasts (type 3; Figure 5a,b; [13]).

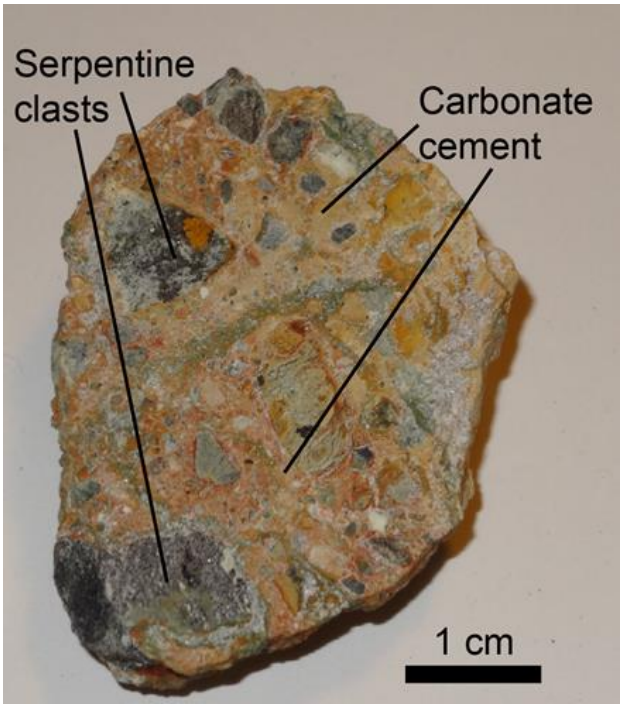

Figure 3. ODP Leg 210 Site 1277 4R-1 77–81 cm sample. Angular to rounded clasts of serpentinite are surrounded by a carbonate cement.

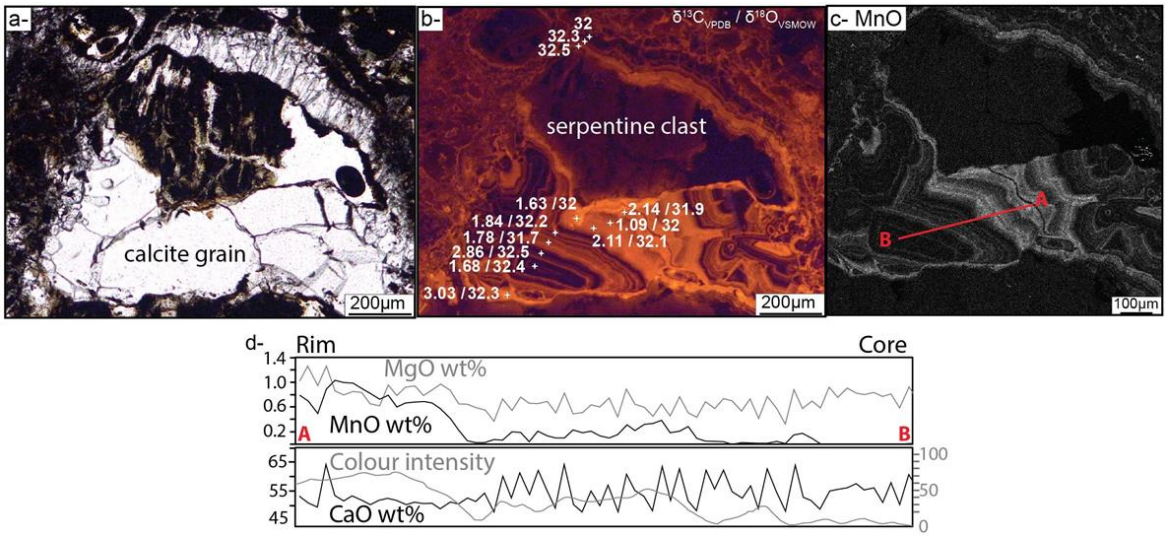

Figure 4. ODP Leg 210 Site 1277 4R-1 77–81 cm sample. (**a**) Calcite vein in serpentinite clast and (**b**) its cathodoluminescence equivalent (light orange corresponds to a high Mn concentration whereas dark red is associated with low Mn concentrations). (**c**) Microprobe map of MnO of the same area. (**d**) Microprobe profile of CaO, MgO and MnO versus the color intensity along the profile A, B shown by the red line in c. White crosses: data points of measured δ $^{18}O_{SMOW}$ and δ $^{13}C_{VPDB}$.

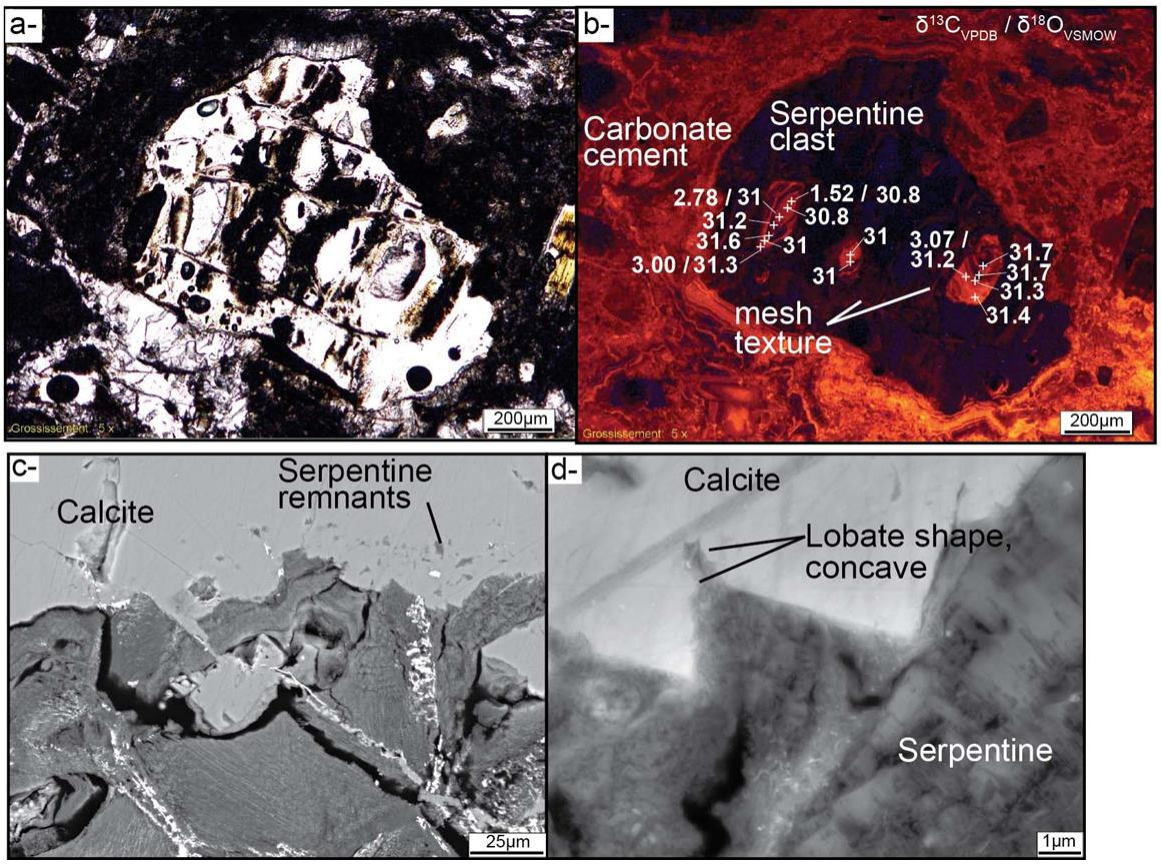

Figure 5. ODP Leg 210 Site 1277 4R-1 77–81 cm sample. (**a**) Serpentine core mesh replaced by carbonate and (**b**) its cathodoluminescence equivalent (light orange corresponds to a high Mn concentration whereas dark red is associated with low Mn concentrations). White crosses: data points of measured δ $^{18}O_{SMOW}$ and δ $^{13}C_{VPDB}$. (**c**,**d**) SEM images of calcite replacing serpentine.

In cathodoluminescence (CL) images, the calcite veins (type 1) display a color banding with an alternation of black and orange (Figure 4b). The banding is either parallel to fracturing, showing the opening direction of the vein (Figure 4b), or concentric, leading to scalenohedral crystals (Figure 5b). New grains appear to have nucleated in the vein at fracture edges, leading to single crystals with irregular shapes and low Mn-content (Figure 4d; dark in CL image). In addition, calcite grain growth occurs in parallel to the fracture opening direction (Figure 4b). It is common to observe in CL that the cores of the scalenohedron-shaped calcites are black (Mn-poor) whereas the last band is the brightest (Mn-rich; up to 1 wt. %, Figure 4d). The scalenohedral sparitic calcite grains found in veins vary in size from 10 to 100 μm. The banding in the veins display sharp contacts with the calcite in the cement due to brecciation (Figure 4c). The cement (type 2) is characterized by small, grain-sized calcite (<50 μm), with no CL-banding; CL colours are dark orange, with neither variation at sample or core scale (Figures 4b and 5b).

The serpentinite clasts are made of a network of mesh-like, regularly spaced fractures with two perpendicular orientations. Within the core of this regular mesh texture, 50 to 200 μm wide calcite grains are found (type 3) (Figure 5a,b). The mesh texture is preserved during replacement by carbonates (i.e., pseudomorphic replacement). In the core of the mesh, calcite grains grow concentrically from a nucleus, until reaching the rim of the mesh (Figure 5b). Depending on the nucleus location, the bands may not be continuous in the calcite grain. The CL colour of the bands is dark near the nucleus and again, bright orange in the outermost one (Figure 5b).

The banding observed in calcites of types 1 and 3 is similar (Figures 4b and 5b). At the contact between calcite and serpentine, the calcite grains are sharp and angular above the μm-scale (Figure 5c,d), and below the μm-scale the grains can display lobate shapes and are concave towards the serpentine (Figure 5d). The reaction front separates the well-crystallized calcite and fibrous serpentine and spans several micrometers. It is composed of <0.5 μm-thick calcite needles pervasively distributed in a disordered serpentine matrix (Figure 5d).

The μm-scale banding does not allow us to perform bulk isotopic analysis, as we would have obtained a mean value for all the bands. Therefore, we measured in-situ $\delta^{18}O$ in the different bands with the SIMS. We acquired profiles through calcite grains in veins (type 1) and in the serpentine mesh core (type 3). Only CL bands larger than 20 μm could be analyzed (white crosses on Figures 4b and 5b; Table S2). Measured $\delta^{18}O_{VSMOW}$ values cluster in a relative restricted range for pseudomorphous grains (30.8 ± 0.4‰ to 32.6 ± 0.4‰, n = 14), whereas calcite in veins are homogeneous (28.4 ± 0.4‰, n = 49) (Figure 6; Table S2). In all the calcites measured, no variation of $\delta^{18}O_{VSMOW}$ can be observed from core to rim. $\delta^{13}C_{VPDB}$ measurements vary from 1.09 ± 0.63‰ to 3.07 ± 0.85‰ (Table S2) but do not show systematic variation with the Mn-banding. Our dataset sits within the range of measurements available for the Iberia margin (Figure 6).

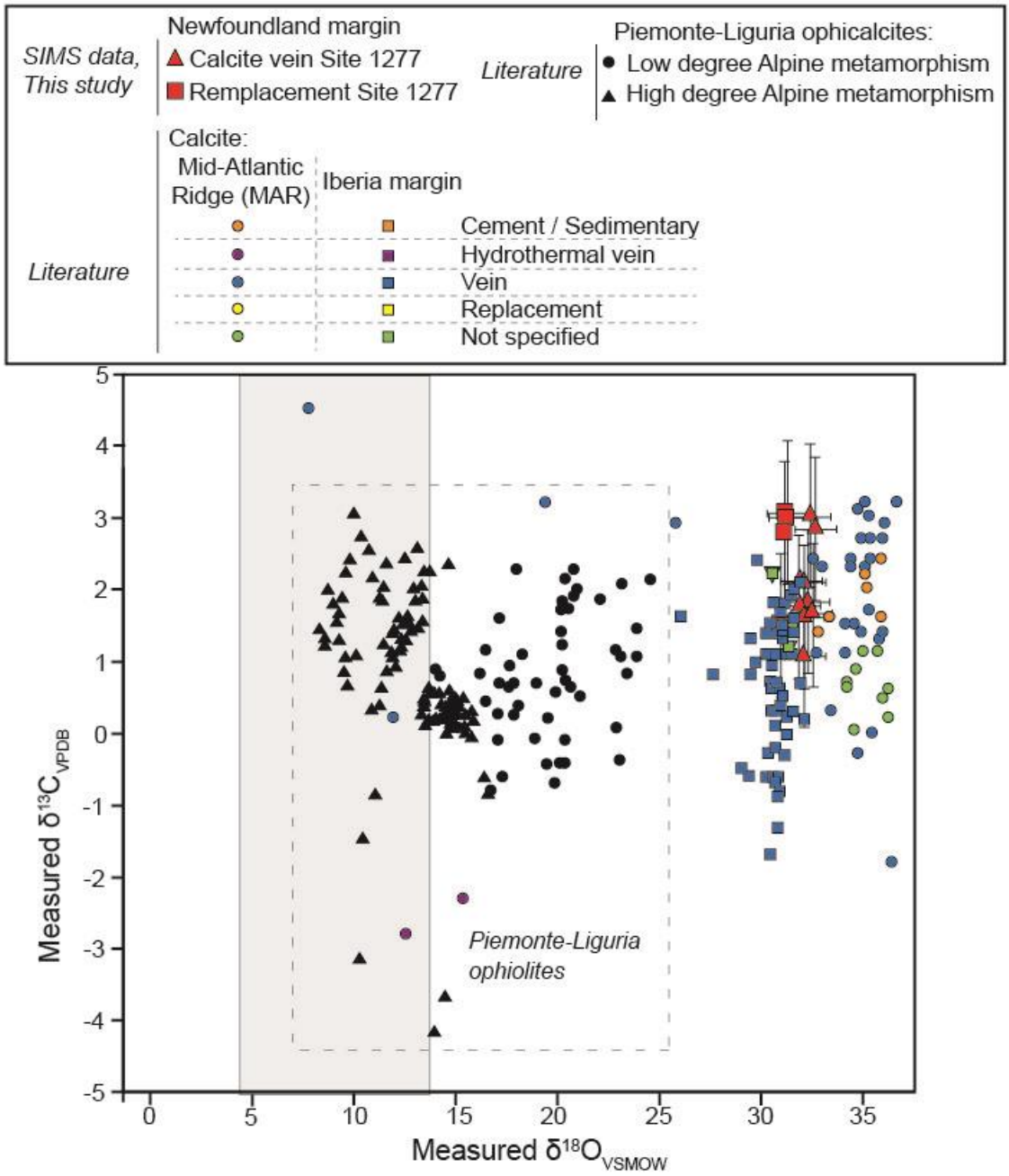

Figure 6. Diagram of $\delta\ ^{18}O_{SMOW}$ versus $\delta\ ^{13}C_{VPDB}$ measured with the Secondary Ion Mass Spectrometer (SIMS) facility compared to compilation of literature data of ophicarbonates from the Newfoundland-Iberia (NF-I; squares) margin, Mid-Atlantic Ridge (MAR; circles) and Alpine ophiolites, affected by low metamorphism degree (black circles) and high metamorphism degree (black triangles). See references in Table S1.

4.2. Thermodynamic Modeling of Carbonation

Opposite flow directions in the recharge and the discharge models are responsible for the formation of different mineralogical assemblages (Figures 7 and 8) and aqueous fluid compositions (Figures 9 and 10). This is due to the variations in mineral solubility with temperature. If mineral solubility increases with temperature (silicates), fluid transfer from low to high temperature (recharge) will lead to dissolution, whereas fluid transfer from high to low temperature (discharge) will lead to precipitation. Therefore, mass transfer will differ for models considering recharge or discharge. An opposite trend is

expected for minerals with solubility decreasing with temperature (carbonates). Rock composition is observed to change along sharp boundaries (reaction fronts) for both recharge (Figure 7) and discharge models (Figure 8). In both models, the initial serpentine, exclusively composing the rock, is progressively replaced by talc as the fluid circulates through the rock. The talc is ultimately replaced by quartz (or clays at temperatures below ca. 40 °C) for the largest amount of fluid having circulated through the rock. The mineralogical assemblage can thus become quartz + carbonate and the modelled rock is a listvenite. Talc appears for lower $(W/R)_d$ when the precipitation of Mg-carbonates is allowed in the model, than when Mg-carbonates precipitation is excluded (Figures 7 and 8). These mineralogical evolutions require that the Mg and Si initially contained in serpentine are transported outside the rock as aqueous species in the fluid (Figures 9 and 10).

Carbonates are only formed at temperatures below 150 °C for the discharge model, and 100 °C for the recharge model (Figures 7 and 8e–h). In the discharge model, Ca concentration in the fluid slightly increases from 1.1×10^{-4} to 4.5×10^{-4} mol/kg as temperature decreases. The limitation of the carbonate stability field is thus mainly associated with pH decrease from 8.5 to 5 as temperature increases from 4 to 250 °C (Figure 10). In the recharge model, the limitation of the carbonate stability field is associated with anhydrite ($CaSO_4$) formation at temperature above 100 °C as shown, for example in Figure 9a, with the simultaneous increase in Ca and decrease in HCO_3^- concentrations at ~70 °C. Anhydrite formation only occurs in the first box of the model at high temperature in the discharge model (250 °C).

The distribution and composition of carbonates are different, even though the reactions of serpentine alteration were similar for discharge and recharge. The carbonates are first formed at the lowest temperature (4 °C) in the recharge model (Figure 7b,f). As fluid/rock interactions increase, the precipitation front progressively migrates towards higher temperatures. This front forming a serpentine + carbonate assemblage in equilibrium with a fluid of low Si concentration (Figure 9) is followed by a second front of talc + carbonate precipitation leading to increase in carbonate modal contents up to 60 mol. % (Figure 7h) and in Si concentration up to one order of magnitude (Figure 9h). Carbonates first replace serpentine at high temperatures (~150 °C) in the discharge model compared to the recharge model where this replacement starts at the lowest temperature (4 °C). The modal amounts of carbonate in the boxes are found to progressively decrease along the fluid flow path by one order of magnitude from 150 °C to 50 °C. Serpentine replacement by carbonates requires larger amount of fluids (or larger porosities for the same number of time steps in our model) to be observed in the case of recharge than in the case of discharge. This is due to the higher serpentine solubility where serpentine dissolution occurs in the discharge model at 150 °C than in the recharge at 20 °C. When Mg-carbonate precipitation is included in the model, carbonates are dolomite in the whole investigated temperature range in the recharge model and at temperatures below 20 °C in the discharge model. At temperatures above 20 °C, carbonates precipitate as magnesite in the discharge model, suggesting that Ca-rich carbonates are preferentially formed at low temperature. When Mg-carbonate precipitation is excluded, Ca-carbonates are only found to precipitate in the recharge model at temperatures below 110 °C (Figure 7).

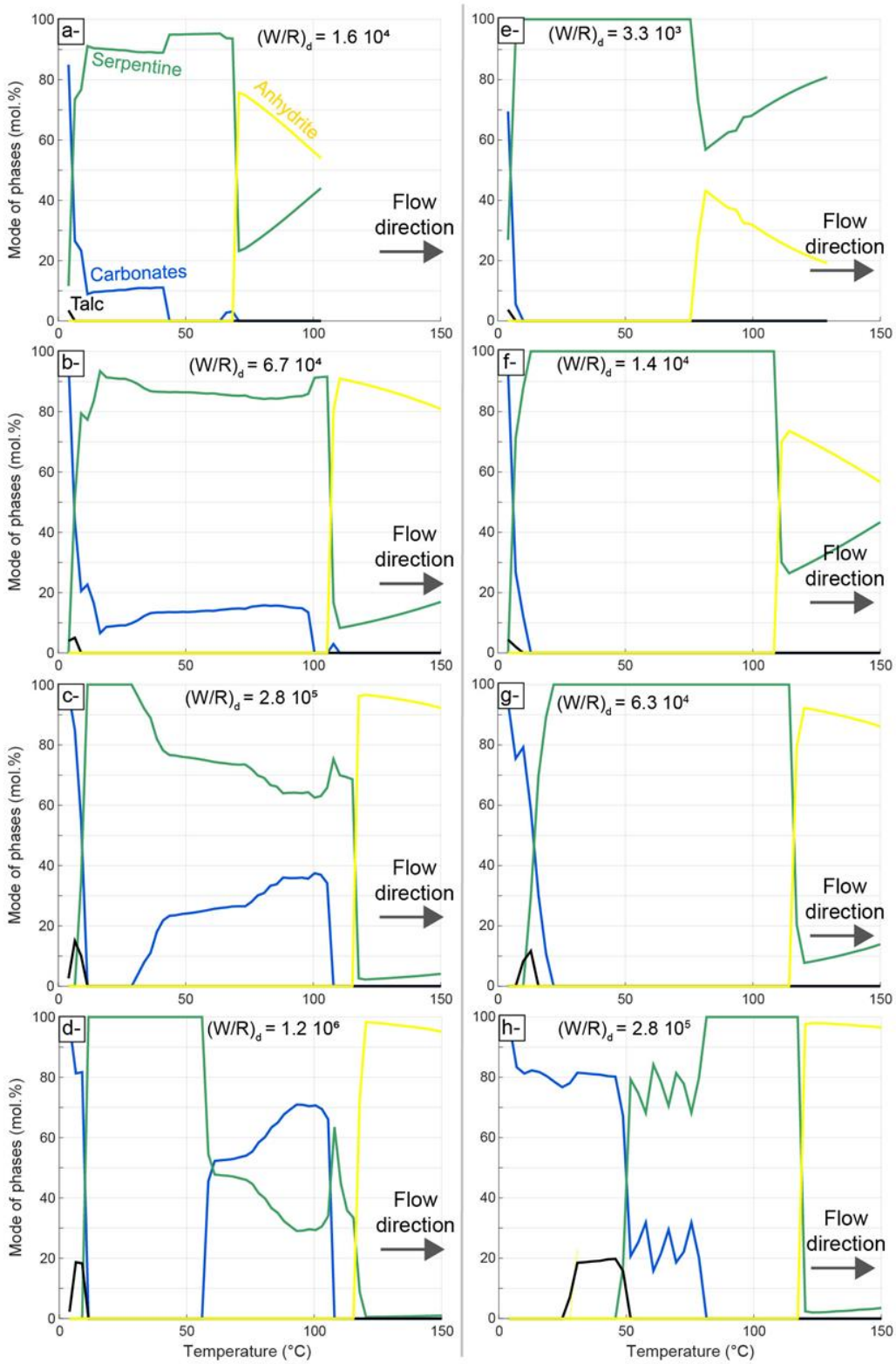

Figure 7. Serpentine (green), carbonates (blue), talc (black) and anhydrite (yellow) modes as a function of temperature in the model for recharge (flow direction is indicated). The model on the left (**a**–**d**) does not include Mg-carbonates whereas the model on the right does (**e**–**h**). For each model, the modes are displayed at various dynamic water to rock ratios $(W/R)_d$. Note that carbonates are first produced at low temperature in a reaction zone progressively extending towards higher temperatures. Carbonate formation is not predicted at temperature above 100 °C where anhydrite is the main Ca-bearing mineral to precipitate.

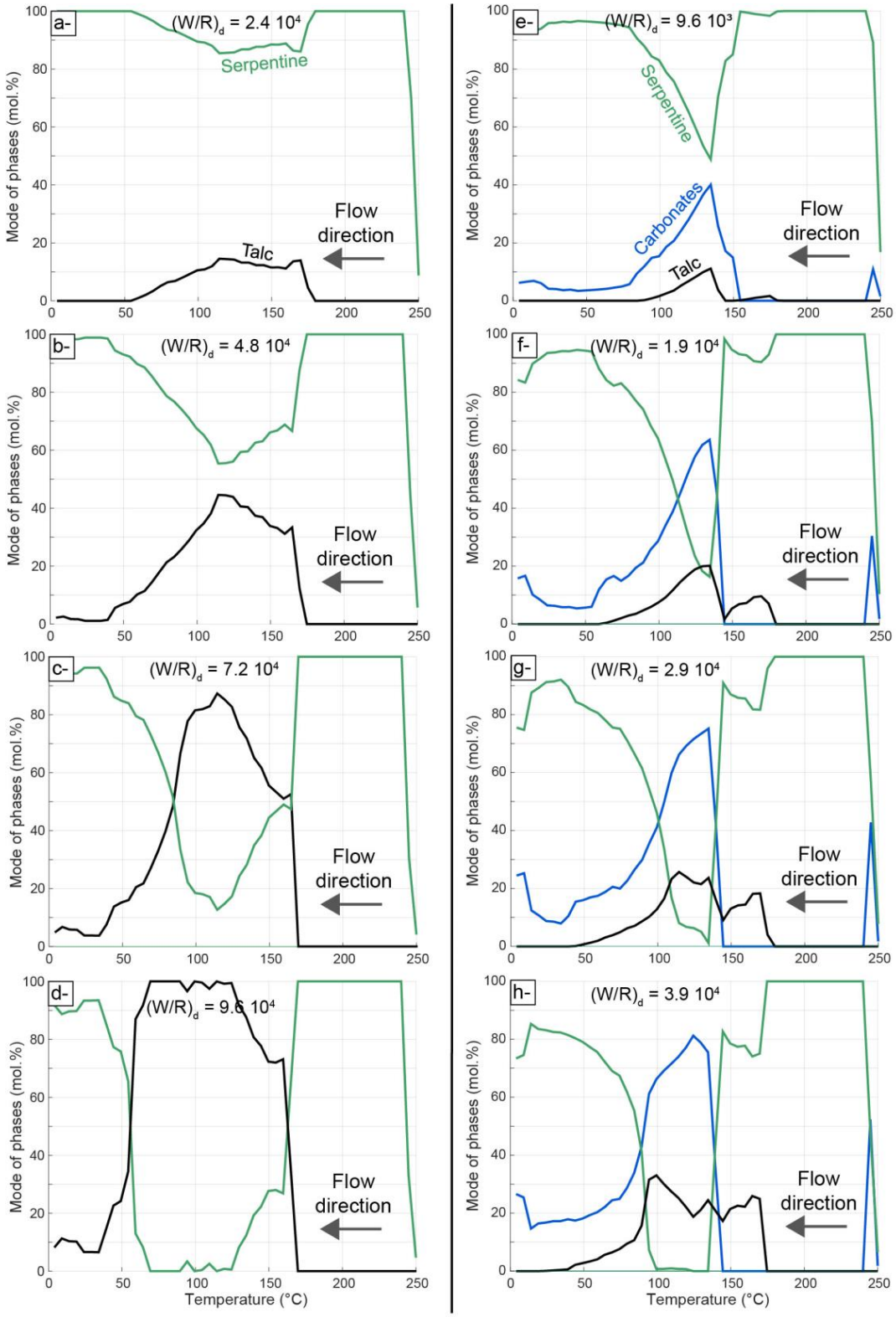

Figure 8. Serpentine (green), carbonates (blue) and talc (black) modes as a function of temperature in the model for discharge (flow direction is indicated). The model on the left (**a**–**d**) does not include Mg-carbonates whereas the model on the right does (**e**–**h**). For each model, the modes are displayed at various dynamic water to rock ratios $(W/R)_d$. Note that Mg-carbonates are mainly produced at temperatures below 150 °C in the model allowing for Mg-carbonate precipitation whereas carbonates are not produced in the model in which Mg-carbonate precipitation is not allowed.

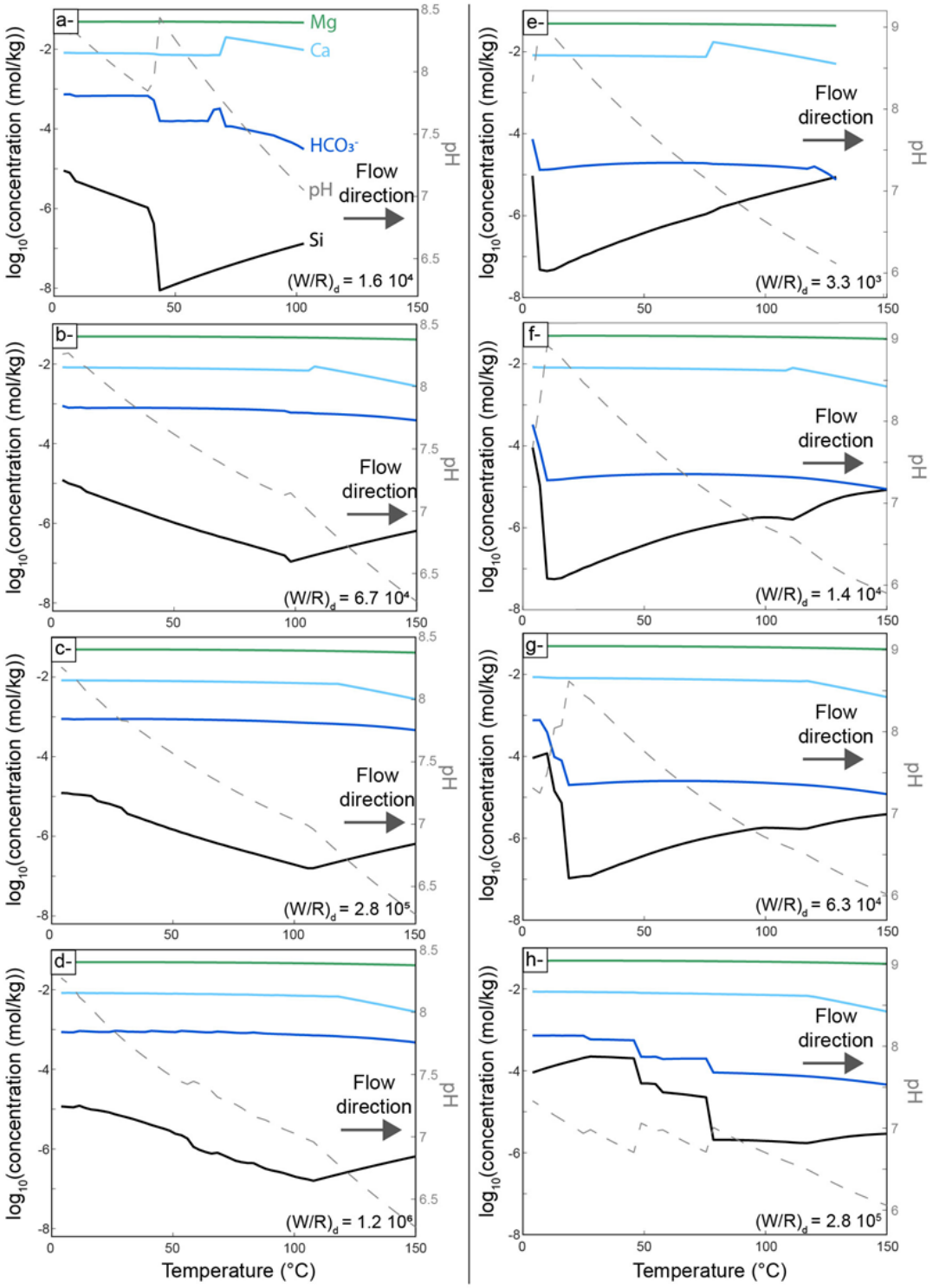

Figure 9. Si (black), Mg (green), Ca (light blue) and HCO_3^- (dark blue) concentrations in the fluid and pH (dashed line) as a function of temperature in the model for recharge (flow direction is indicated). The model on the left (**a**–**d**) does not include Mg-carbonates whereas the model on the right does (**e**–**h**). For each model, concentrations and pH are displayed at various dynamic water to rock ratios $(W/R)_d$.

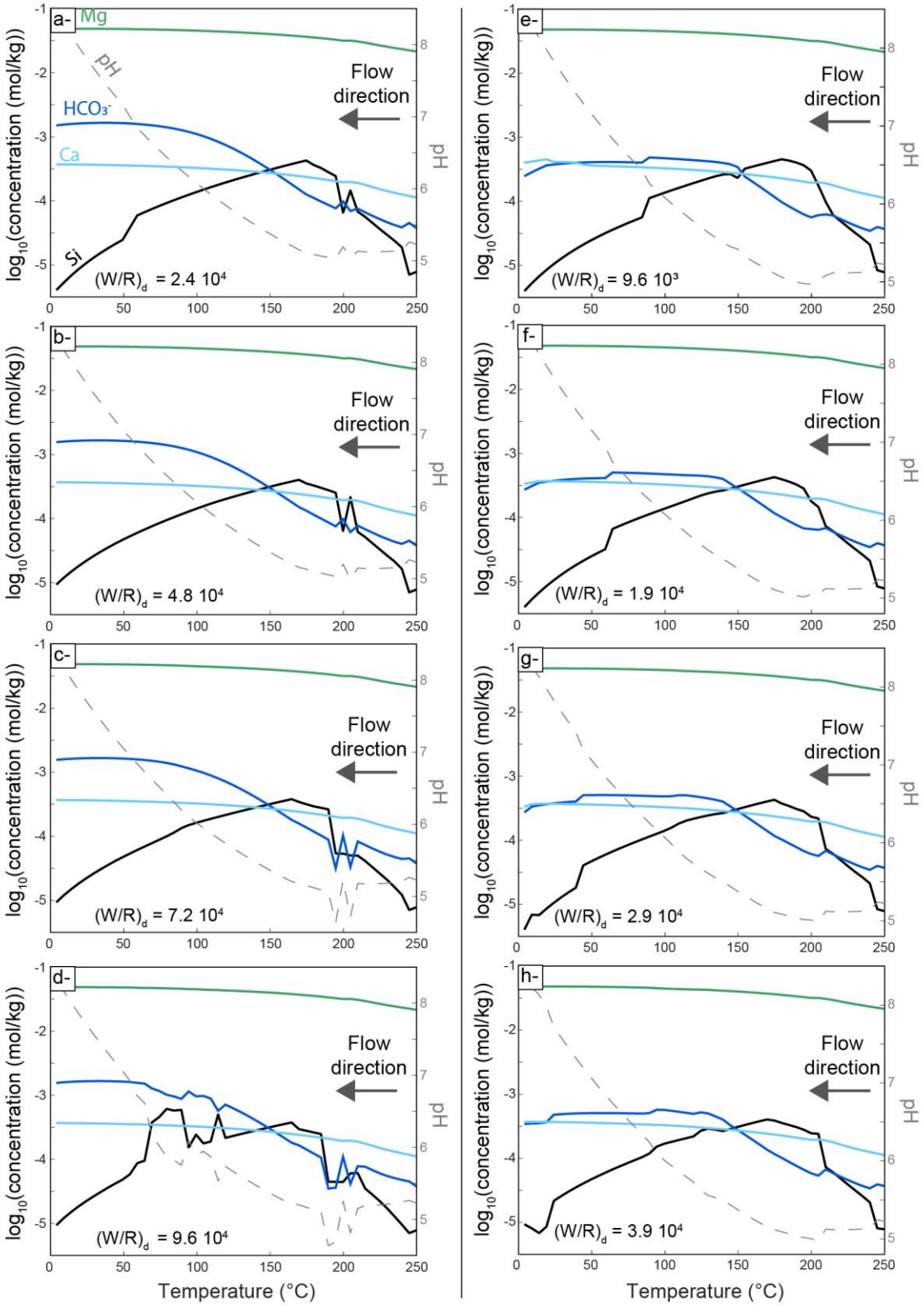

Figure 10. Si (black), Mg (green), Ca (light blue) and HCO_3^- (dark blue) concentrations in the fluid and pH (dashed line) as a function of temperature in the model for discharge (flow direction is indicated). The model on the left (**a**–**d**) does not include Mg-carbonates whereas the model on the right does (**e**–**h**). For each model, concentrations and pH are displayed at various dynamic water to rock ratios $(W/R)_d$.

5. Discussion

5.1. Serpentine Replacement by Carbonate During Seawater Influx in the NF Margin

We identify three mechanisms of carbonation in the Newfoundland serpentinites: veining, cementation and pseudomorphic replacement. Tectonic deformation during mantle exhumation along passive rifted margins leads to cataclasis in the footwall of detachment faults [32] and to fluid circulation. Both mechanisms result in calcite vein formation (e.g., [5,60]). They follow the pre-existing fracture network of the serpentinized peridotite. Near the seafloor, sedimentation is active, leading to calcite cementation into serpentinite breccia. All along this tectono-sedimentary sequence, serpentine is partially replaced by carbonate in the core of the mesh texture. To determine when replacive carbonation occurs during the mantle exhumation, we measured the temperature record of calcite in the inferred oldest carbonate.

During mantle exhumation, the anisotropic thermal contraction of peridotite together with tectonic stresses generates a primary microfracturing responsible for the onset of serpentinization [61]. This fracture network is then re-used for reaction induced fracturing [56,62,63]. The serpentine growing along the microfractures is organized in lizardite pseudocolumns constituting the rim of the mesh texture [61,63,64]. For higher reaction degree, preserved olivine grains can be altered into isotropic serpentine or proto-serpentine [65,66]. The core of meshes can be composed of either preserved olivine or proto-serpentine, depending on the extent of the serpentinization reaction. Residual olivine grains are extremely rare in the Iberia and Newfoundland exhumed serpentine basement, where the degree of serpentinization is >90% complete [67]. Therefore, the different habits of serpentine crystals and their coherence is probably responsible for the preferential carbonate growth in the mesh core of the studied sample. The lobate shape of calcite grains suggests serpentine replacement. Our interpretation is reinforced by the fact that calcite needles at the reaction front start to grow from isotropic serpentine. In the veins, calcite grains grow with a similar CL banding, but the absence of lobate shape suggests that these grains are not replacive.

Hydrothermal systems are an important source of manganese as described in several present-day active hydrothermal vents, e.g., East Pacific Rise, [68] or in the acidic hydrothermal systems (pH < 5) from the MAR where Mn concentration varies from 59 to 2250 µM [18]. Ca^{2+} from calcite can be substituted by Mn^{2+} to form a solid solution of $MnCO_3$ and $CaCO_3$ [69]. CL of calcite is activated by Mn^{2+}, whose emission colour is orange [70]. Temperature is not strongly influencing the Mn uptake in calcite grains [71]. Therefore, the Eh-dependent solubility of Mn into the fluid allows using CL colour variation as a proxy for oxygen fugacity variations in the fluid [72].

The CL-banding sequence is comparable between calcite grains growing in veins and in the serpentine mesh core, indicating a synchronous growth. The low content of Mn in calcite grains core reflects oxidizing conditions in both cases. In contrast, the last band in calcite is enriched in Mn testifying for more reduced fluids [72]. The fluid responsible for carbonation is oxidizing from the beginning of the reaction, even though fluids formed during serpentinization are reduced due to the coupled oxidation of the ferrous iron from olivine and pyroxenes to form magnetite [73]. This indicates that carbonation, from its onset, occurs after serpentinization near the seafloor, through interaction with oxidizing seawater.

The measured $\delta^{18}O$ are homogeneous in calcite precipitating in the veins ($\delta^{18}O_{VSMOW} \approx 31‰$) and vary by less than 2‰ in the calcite formed in the cores of the serpentine meshes. There is no systematic variation in the $\delta^{18}O$ with respect to the Mn content variation or the location in the grain. The narrow ranges of the in-situ isotopic measurements at the tens of micrometer scale indicate limited variations of the composition of infiltrating fluids, both spatially, as suggested by the bulk data at MORs, and temporally, as indicated by the absence of zoning. Assuming seawater isotopic composition, the $\delta^{18}O$ measurements give carbonation temperatures between T_{min} −1 to 11 °C and T_{max} 4 to 18 °C (Table S2). This low temperature of carbonate formation is consistent with experiments of inorganic carbonate precipitation at 25 °C [74–76]. It also suggests that serpentinization and carbonation can be two

temporally decoupled processes. Indeed, the highest serpentinization rates measured in experiments are found in the range of 250–300 °C [77,78].

The temporal decoupling between serpentinization and carbonation can also be shown by subtracting $\delta^{18}O_{calcite}$ from $\delta^{18}O_{serpentine}$ [79]. For this calculation, we used a mean value calculated from a compilation of $\delta^{18}O_{serpentine}$ from the Iberia margin (Leg 103, [34]; Leg 149, [3]) and from MAR [80]. The mean value for $\delta^{18}O_{serpentine}$ used here is 10.65‰. We also used a mean value for $\delta^{18}O_{calcite}$ from the NF margin i.e., 31‰. If calcite was formed in equilibrium with serpentine, $\delta^{18}O_{calcite}$–$\delta^{18}O_{serpentine} \approx 10$‰. Here, the difference exceeds 20‰ (Figure 6 and Table S2), therefore, calcite and serpentine are not at equilibrium. Fast advective fluid transport (e.g., in a fracture network) during fluid recharge or discharge would lead to limited interaction between the fluid and the serpentine, and to the preservation of the fluid isotopic signature. However, pervasive fluid flow in a low permeable rock favors the fluid–serpentine interactions and can thus modify the initial isotopic signature of the fluid and of the precipitating carbonate [81]. In addition to the fluid–serpentine disequilibrium, the extensive carbonation as well as the absence of $\delta^{18}O$ zoning in calcite indicate that carbonation is fluid-buffered. As the fluid has a seawater signature, carbonation probably occurs near the surface during the onset of recharge into the serpentinized peridotites. The reproducibility of data in the MAR and Iberia-Newfoundland margins suggests that the recharge is a common process.

$\delta^{13}C_{VPDB}$ measured in NF margin are in agreement with previous data from the conjugated Iberia margin (i.e., between −3‰ and 3‰) and are typical for marine hydrothermal systems (e.g., [1]). This suggests that C is dominantly inorganic derived from seawater as suggested for the Iberian margin [1]. Thermodynamic modeling indicates that such a precipitation of seawater-derived inorganic carbon is possible and requires the circulation of more than 10^3 kg of seawater per kg of rock (Figures 7 and 8). The need for high dynamic water to rock ratios is associated with the low concentration of inorganic carbon in seawater (~2 mM). There are no systematic correlations between Mn-banding and $\delta^{13}C$ variation.

5.2. Carbonation in Passive Margins and Slow-Spreading MORs

We compiled calcite $\delta^{18}O$ and $\delta^{13}C$ bulk measurements from the Iberia and Newfoundland margins and from the Central MAR ophicarbonates (Figure 6). Based on their $\delta^{18}O$ record and calculated temperatures of formation, we infer that the ophicarbonates can be separated into two distinct groups, (1) calcite formed during seawater influx in an evolving carbonation front; or (2) during hydrothermal fluid discharge, in the case that during recharge, fluid-peridotite interaction was small.

As calcites from the Iberia margin and MAR, formed by veining, cementation and pseudomorphic replacement, record high $\delta^{18}O$, we infer this calcite to be formed during seawater influx. This has already been proposed in calcite veins from Iberia with O isotopic compositions varying from 27.6‰ to 31.2‰ [1] and in sedimentary carbonates (e.g., botryoidal calcite) at the Iberia margin ($\delta^{18}O$ from 30‰ to 32‰; [2,35]) and in the MAR ($\delta^{18}O$ from 33‰ to 35‰; [23]).

Calcite formed during hydrothermal fluid discharge is created by veining or hydrothermal deposits (e.g., [21,23,24]). In the MAR, carbonates found in veins and deposits are calcite and aragonite [21]. Mg content in calcite can be as high as 28 wt. % [24]. These high temperature calcite veins are found at the vicinity of hydrothermal vents, and record $\delta^{18}O$ between 26‰ and 8‰ (Mid-Atlantic Ridge, Kane Fracture Zone [26]; ODP Leg 209, [27]; Lost City, [21,23]). However, those samples represent a minority of the collected samples (see references in Table S1). Such low $\delta^{18}O_{calcite}$ indicates carbonation temperatures higher than 100 °C [23]. No pseudomorphic replacement is observed in environments in close relationship with an active hydrothermal vent. Based on O and C isotopic signature of replacive calcites, we interpret carbonate replacement in the samples from Newfoundland, the Iberian margin and the MAR as related to near-surface alteration during seawater influx.

We demonstrate that carbonation on passive margins is a low temperature, near surface process. This is true, even if magmatism is present as demonstrated at Site 1277, where syn- and post-rifting magmatism was identified (e.g., [39]). Indeed, calcite recorded temperatures below 20 °C. In the case

of the Iberia-Newfoundland margins, magmatism has also no effect on the isotopic record, and hence does not influence carbonate precipitation.

5.3. Insights from Numerical Modeling

Carbonates are formed at two distinct temperature ranges at MORs, either below 10 °C or locally at the Lost City above 100 °C in veins feeding hydrothermal vents. Interestingly, this difference in carbonation temperature is also the main difference between the two simulations performed here with recharge and discharge models. Our simulations reproduced carbonate formation during recharge at near-surface conditions. They also predict carbonate formation at approximately 150 °C during discharge. Moreover, carbonate production required a higher fluid amount ($(W/R)_d$) for recharge than for discharge models, suggesting more open system conditions. Talc formation is decoupled from carbonate precipitation in the recharge models only, leading to rocks exclusively composed of serpentine and carbonates as observed in the natural samples. In all the simulations, Ca-rich carbonates were only formed at low temperature, whereas carbonation at temperature above 150 °C only produced Mg-rich carbonates. Based on these results, we interpret carbonate replacement in the samples from Newfoundland, the Iberian margin and the MAR as related to near-surface alteration during recharge. Carbonation at high temperature (>100 °C; [23]) is also expected to occur at MORs during discharge and, in particular, near hydrothermal vents such as the Lost City. The simulations predict the observation of calcite in the natural samples studied here, but they do also predict Ca-rich carbonates formation at temperatures above 100 °C, as is observed at the Lost City Hydrothermal Field. Due to missing compatible thermodynamic data, we do not include phases such as layered double hydroxides (coalingite-pyroaugite, LDHs), and hydrous Mg-carbonates (hydromagnesite and nesquehonite) (e.g., [82]).

5.4. Implications for Ophicarbonates Formation Preserved in Ophiolites

Ophicarbonates have been described first in remnants of the central Jurassic Tethys, in the Klosters, Totalp and Arosa ophiolites, in the Central-Eastern Alps [4] and in the Chenaillet ophiolite in the Western Alps [9]. Over the last 30 years, multiple studies have been conducted with a renewed interest, since they contain a key to the understanding of mantle exhumation to the seafloor, and because of their implication as an analogue for present-day passive margins. In addition, carbonation of serpentinite and other mantle rocks is a potential engineering solution to CO_2 sequestration [83]. Alpine ophicarbonates are interpreted to be the result of oceanic alteration of serpentinized peridotites during mantle exhumation associated with the Jurassic hyperextension phase [13], already proposed by Weissert and Bernoulli [4] and discussed by Früh-Green et al. [84].

It is important to note that carbonates are mostly calcites, and minor aragonite [2], never dolomite. Mineralogy of carbonates encountered in the Alpine Tethys ophicarbonates is mostly calcite, and minor dolomite (e.g., in Val Ventina, Alps, [82]; and in the Chenaillet, [13] and references therein). We compiled $\delta^{18}O$ and $\delta^{13}C$ measured in ophicarbonates from the literature in several locations in the Alpine Tethys. The data set contains bulk measurements on carbonate veins [84], disseminated carbonates [13], as well as sedimentary ophicarbonates [4,85,86].

Regional metamorphism experienced by ophicarbonates in the Platta nappes did not exceed 200 to 250 °C ([87] and references therein). The $\delta^{18}O$ values of carbonates range from 21‰ to 14‰ [85] in ophicarbonates towards the thrust plane, which separates them from serpentinites in the Platta nappe. Metamorphism and fluid flow during metamorphism seems to play in important role in the $\delta^{18}O$ record in ophicarbonates, and hence a careful re-evaluation of these values should be attempted to ascertain the initial condition of formation of these carbonates prior to metamorphism.

This explanation is supported by the low $\delta^{18}O$ values also recorded in sedimentary ophicarbonates (from 8.6‰ to 24.7‰ in the Western and Central Alps [4,13,86,88]). These low $\delta^{18}O$ values correspond to temperatures from 40 to 70 °C (Table S1). As in the Iberian margin, near-surface sedimentary carbonation

precipitation also occurs in a range of temperatures below 20 °C, we infer that these temperatures are too high for true sedimentary deposition.

A way to optically verify if carbonate re-equilibration by metamorphism has started is to observe the Mn-banding in carbonates by cathodoluminescence. Diffusion of Mn is approximately 10 orders of magnitude faster (e.g., 1 mm at 300 °C in 25 Ma) than diffusion of O in calcite (30 µm to 10^{-6} µm for the same setting [89–91]. Many carbonates precipitating in shallow hydrothermal settings will obtain rhythmic layers of CL-active elements, as is shown in this study. Since diffusion of these elements (like Mn) is fast, they will disappear upon heating, and are obliterated by recrystallization. This means that if a carbonate preserves its banding structure acquired during carbonation on the seafloor, it should also preserve its $\delta^{18}O$ signature. Therefore, a test for recognizing re-equilibration in ophicarbonates from ophiolites would be the presence of thin CL-banding. This criterion can only be applied if diffusion is the only process acting during re-equilibration since calcite dissolution-reprecipitation may also modify the composition of the carbonates at low temperature. Nevertheless, this will also eliminate potentially the isotopic signature.

To follow up, we estimate the $\delta^{18}O$ expected in calcite that is supposed to be equilibrated with the surrounding serpentine during metamorphism. $\delta^{18}O_{serpentine}$ in Alpine ophiolites ranges from 4.3‰ to 13.4‰ [84]. If calcite and the surrounding serpentine are in equilibrium, according to the temperature of metamorphism reached, $\delta^{18}O_{calcite}$-$\delta^{18}O_{serpentine}$ should be $\Delta^{18}O_{cc\text{-}serp} \approx 5.27‰$ to 5.98‰ for a metamorphism at 200–250 °C (e.g., Platta); and $\Delta^{18}O_{cc\text{-}serp} \approx 2.82‰$ to 3.41‰ for a metamorphism at 450–550 °C (e.g., Val Ventina; [79]). Our compilation shows that samples displaying the least degree of metamorphism have $\Delta^{18}O_{cc\text{-}serp}$ higher than the estimated equilibrium values; whereas samples displaying the highest degree of metamorphism have $\Delta^{18}O_{cc\text{-}serp}$ corresponding to the estimated calcite–serpentine fractionation.

An alternative to the onset of differential re-equilibration during Alpine metamorphism could be that instead of precipitating during seawater influx, the ophicarbonates were formed during hydrothermal fluid discharge. We want to emphasize that this explanation would explain only the high temperatures recorded by the $\delta^{18}O$ in carbonates, as the textures and brecciation processes are similar to the present-day passive margin samples and are easily explained by the seawater influx model.

In an ophiolite where hydrothermal vents are clearly observed (e.g., Chenaillet), it should be easier to establish a relationship between carbonation and the distance between the hydrothermal fluid pathways. Magmatism may also play an important role in the high temperature recorded by ophicarbonates in distal parts of the Ocean Continent Transitions such as the Chenaillet, as late syn-rift to early post-rift magmatism with intrusions crosscutting the detachment faults are observed [28].

In the case of mostly discharge-driven carbonation, as the Alpine Tethys ophicarbonates are a good analogue for the present-day Iberia passive margin, near-surface ophicarbonates with high $\delta^{18}O$ (25–35‰) should also be reported in the remnant ophiolites, which is still not the case.

5.5. Implications for CO_2 Mineral Sequestration

The storage of CO_2 through carbonate precipitation appears to be one of the solutions to compensate for the anthropogenic greenhouse gas emissions [92]. Among the Earth's crust rocks, ultramafic rocks have one of the highest potentials for carbon sequestration due to their high magnesium content [6,93–99]. The results of this study provide constraints for the process of CO_2 sequestration in ultramafic rocks. We show here that low-temperature carbonation on the seafloor (T < 50 °C) produces Ca-carbonates. The calcium source is the seawater, and high water to rock ratios are needed to induce carbonate precipitation. The high MgO content of the ultramafic rock is therefore not an asset for CO_2 storage in the conditions prevailing on the seafloor. However, thermodynamic modeling indicates that high temperature carbonation (T > 100 °C) requires smaller water to rock ratios since magnesium can be incorporated into the carbonates. Mimicking the high temperature process thus appears to be more relevant to develop an efficient CO_2 storage solution. Such a solution would also need to circumvent the potential issues associated with the modification of the porous network by

carbonation. Serpentine reaction occurring at high temperature to form talc and then quartz indeed requires significant magnesium and silica transport.

6. Conclusions

We provide microtextural observations of pervasive serpentine replacement by calcite and synchronous calcite growth in veins in exhumed mantle from the Newfoundland passive margin. We interpret those calcite grain cores as the first carbonate to grow in exhumed mantle. This is shown by the crosscutting relationship between brecciation and calcite grains textures revealed by CL images. Replacive calcite maintains the serpentine mesh texture and grows as scalenohedral crystals with a characteristic Mn-compositional banding. Preciseness of SIMS allowed us to measure O and C isotopic composition of each band in a single calcite grain. Measured O isotopes highlight no systematic variation, C isotope measurements display seawater range values and O isotope thermometry reveals that carbonation is cold (<20 °C) since the onset of the reaction.

Our thermodynamic modeling predicts Ca-rich carbonate crystallization near-surface during seawater influx and hydrothermal fluid discharge. Si-rich phases appear in the system with carbonation front evolution through time and space (e.g., talc).

In the discharge model, this stability field limitation is associated with carbonate dissociation into $HCO_3^-{}_{,aq}$ as the pH decreases with temperature. In the recharge model, the limitation of the carbonate stability field is associated with anhydrite ($CaSO_4$) formation at temperatures above 100 °C. Anhydrite formation only occurs in the first box of the model at high temperature in the discharge model (250 °C). We summarize the petrological, geochemical and numerical modeling results of this study in Figure 11, where the differences between recharge and discharge regarding carbonate precipitation are highlighted.

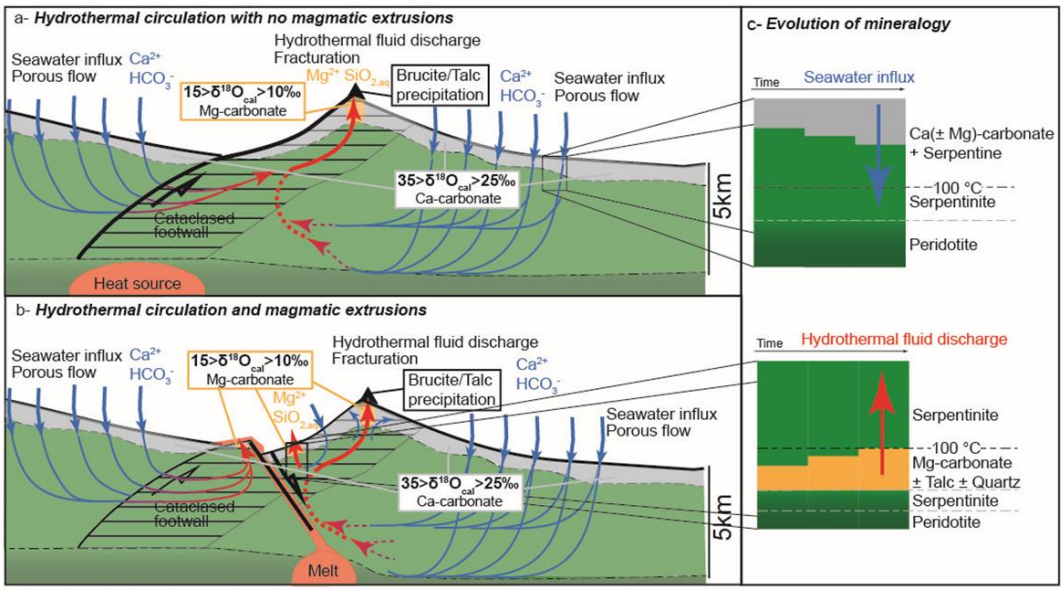

Figure 11. Conceptual model for the relationship between carbonation, hydrothermal circulation and magmatism. Two different models are proposed without (**a**) and with (**b**) magmatic extrusions. They both include recharge and discharge zones. Low-temperature carbonation (<50 °C) occurs in the recharge zones leading to Ca(±Mg)-carbonate formation (**c**). High-temperature carbonation starts at 150 °C in the discharge zones where Mg-carbonates only precipitate (**c**). Carbonation induces more magnesium and silica transport in the discharge zones leading to serpentine replacement by talc and then quartz as the water to rock ratio increases. These elements may precipitate at the surface in hydrothermal chimney as it is observed at the Lost City Hydrothermal Field [23]. The discharge model requires large scale fluid transport in permeable zones whereas carbonation in the recharge model is widespread and occurs through pervasive fluid transport.

According to our petrological and modeling results, we wonder why there are no cold ophicarbonates sampled yet in the Alpine ophiolites, and we propose that, in the case of absence of post-rift melting, O and C isotopic composition might have been re-equilibrated during Alpine deformation.

We show that carbonation of ultramafic rocks is more efficient (lower water to rock ratio) at high temperature (>100 °C) since Mg-bearing carbonates can be formed. This result may guide the development of future engineering solutions for CO_2 sequestration.

Supplementary Materials: The following are available online at http://www.mdpi.com/2075-163X/10/2/184/s1; Table S1: Compilation of carbon and oxygen isotope composition on calcite in serpentinized peridotites collected on the seafloor and in metamorphic environments. Table S2: Carbon and oxygen isotope composition on calcite from IODP Site 1277. Table S3: Electron microprobe analyses of serpentine and carbonate, and seawater composition used in thermodynamic modeling.

Author Contributions: S.P. and B.M. contributed to the data acquirement, interpretation of the data and wrote the article; L.B. contributed to the interpretation; A.-S.B. contributed to the setting of the SIMS. All authors have read and agreed to the published version of the manuscript.

Funding: Suzanne Picazo acknowledges Center of Excellence in Basin Analysis Grant from ExxonMobil for financial support. Benjamin Malvoisin acknowledges support from the Swiss National Science Foundation (Ambizione grant n°PZ00P2_168083). Lukas Baumgartner obtained funding from Swiss National Science Foundation and KIP6 PCI CASA.

Acknowledgments: The authors are grateful to Tiffany Barry for language corrections. We thank Susanne Seitz and Guillaume Siron for SIMS technical support.

Conflicts of Interest: The authors declare no conflict of interest.

References

1. Schwarzenbach, E.M.; Früh-Green, G.L.; Bernasconi, S.M.; Alt, J.C.; Plas, A. Serpentinization and carbon sequestration: A study of two ancient peridotite-hosted hydrothermal systems. *Chem. Geol.* **2013**, *351*, 115–133. [CrossRef]
2. Morgan, J.K.; Milliken, K.L. Petrography of calcite veins in serpentinized peridotite basement rocks from the Iberia Abyssal Plain, Sites 897 and 899: Kinematic and environmental implications. In *Proceedings of the Ocean Drilling Program, Scientific Results*; Whitmarsh, R.B., Sawyer, D.S., Klaus, A., Eds.; National Science Foundation: College Station, TX, USA, 1996; Volume 149.
3. Agrinier, P.; Cornen, G.; Beslier, M.O. Mineralogical and oxygen isotopic features of serpentinites recovered from the ocean/continent transition in the Iberia Abyssal Plain. In *Proceedings-Ocean Drilling Program Scientific Results*; National Science Foundation: College Station, TX, USA, 1996; pp. 541–552.
4. Weissert, H.; Bernoulli, D. Oxygen isotope composition of calcite in Alpine ophicarbonates: A hydrothermal of Alpine metamorphic signal? *Eclogae Geol. Helv.* **1985**, *77*, 29–43.
5. Clerc, C.; Boulvais, P.; Lagabrielle, Y.; de Saint Blanquat, M. Ophicalcites from the northern Pyrenean belt: A field, petrographic and stable isotopic study. *Int. J. Earth Sci.* **2014**, *103*, 141–163. [CrossRef]
6. Beinlich, A.; Plümper, O.; Hövelmann, J.; Austrheim, H.; Jamtveit, B. Massive serpentinite carbonation at Linnajavri, N-Norway. *Terra Nova* **2012**, *24*, 446–455. [CrossRef]
7. Surour, A.A.; Arafa, E.H. Ophicarbonates: Calichified serpentinites from Gebel Mohagara, Wadi Ghadir area, eastern desert, Egypt. *J. Afr. Earth Sci.* **1997**, *24*, 315–324. [CrossRef]
8. Lavoie, D.; Cousineau, P.A. Ordovician ophicalcites of southern Quebec Appalachians: A proposed early seafloor tectonosedimentary and hydrothermal origin. *J. Sedimentol. Res.* **1995**, *65*, 337–347.
9. Lemoine, M.; Tricart, P.; Boillot, G. Ultramafic and gabbroic ocean floor of the Ligurian Tethys (Alps, Corsica, Apennines): In search of a genetic model. *Geology* **1987**, *15*, 622–625. [CrossRef]
10. Picazo, S.; Cannat, M.; Delacour, A.; Escartín, J.; Rouméjon, S.; Silantyev, S. Deformation associated with the denudation of mantle-derived rocks at the Mid-Atlantic Ridge 13°–15° N: The role of magmatic injections and hydrothermal alteration. *Geochem. Geophys. Geosyst.* **2012**, *13*. [CrossRef]
11. Cannat, M. Emplacement of mantle rocks in the seafloor at mid-ocean ridges. *J. Geophys. Res. Solid Earth* **1993**, *98*, 4163–4172. [CrossRef]
12. Manatschal, G.; Bernoulli, D. Architecture and tectonic evolution of nonvolcanic margins: Present-day Galicia and ancient Adria. *Tectonics* **1999**, *18*, 1099–1119. [CrossRef]

13. Lafay, R.; Baumgartner, L.P.; Schwartz, S.; Picazo, S.; Montes-Hernandez, G.; Vennemann, T. Petrologic and stable isotopic studies of a fossil hydrothermal system in ultramafic environment (Chenaillet ophicalcites, eastern Alps, France): Processes of carbonate cementation. *Lithos* **2017**, *294*, 319–338. [CrossRef]
14. Kelemen, P.B.; Matter, J. In situ carbonation of peridotite for CO_2 storage. *Proc. Natl. Acad. Sci. USA* **2008**, *105*, 17295–17300. [CrossRef]
15. Matter, J.; Kelemen, P. Permanent storage of carbon dioxide in geological reservoirs by mineral carbonation. *Nat. Geosci.* **2009**, *2*, 837–841. [CrossRef]
16. Johannes, W. Experimental investigation of the reaction forsterite + H2O ⇌ serpentine + brucite. *Contrib. Mineral. Petrol.* **1968**, *19*, 309–315. [CrossRef]
17. Mével, C. Serpentinization of abyssal peridotites at mid-ocean ridges. *Comptes Rendus Geosci.* **2003**, *335*, 825–852. [CrossRef]
18. Charlou, J.L.; Donval, J.P.; Fouquet, Y.; Jean-Baptiste, P.; Holm, N. Geochemistry of high H_2 and CH_4 vent fluids issuing from ultramafic rocks at the Rainbow hydrothermal field (36 14′ N.; MAR). *Chem. Geol.* **2002**, *191*, 345–359. [CrossRef]
19. Barreyre, T.; Escartin, J.; Sohn, R.A.; Cannat, M.; Ballu, V.; Crawford, W. Temporal variability and tidal modulation of hydrothermal exit-fluid temperatures at the Lucky Strike deep-sea vent-field, Mid-Atlantic Ridge. *J. Geophys. Res.* **2014**, *119*, 2543–2566. [CrossRef]
20. Cooper, M.J.; Elderfield, H.; Schultz, A. Diffuse hydrothermal fluids from Lucky Strike hydrothermal vent field: Evidence for a shallow conductively heated system. *J. Geophys. Res.* **2000**, *105*, 19369–19375. [CrossRef]
21. Kelley, D.S.; Karson, J.A.; Früh-Green, G.L.; Yoerger, D.R.; Shank, T.M.; Butterfield, D.A.; Hayes, J.M.; Schrenk, M.O.; Olson, E.J.; Proskurowski, G.; et al. A serpentinite-hosted ecosystem: The Lost City hydrothermal field. *Science* **2005**, *307*, 1428–1434. [CrossRef]
22. Lang, S.Q.; Butterfield, D.A.; Schulte, M.; Kelley, D.S.; Lilley, M.D. Elevated concentrations of formate, acetate and dissolved organic carbon found at the Lost City hydrothermal field. *Geochim. Cosmochim. Acta* **2010**, *74*, 941–952. [CrossRef]
23. Früh-Green, G.L.; Kelley, D.S.; Bernasconi, S.M.; Karson, J.A.; Ludwig, K.A.; Butterfield, D.A.; Boschi, C.; Proskurowski, G. 30,000 years of hydrothermal activity at the Lost City vent field. *Science* **2003**, *301*, 495–498. [CrossRef] [PubMed]
24. Ludwig, K.A.; Kelley, D.S.; Butterfield, D.A.; Nelson, B.K.; Früh-Green, G. Formation and evolution of carbonate chimneys at the Lost City Hydrothermal Field. *Geochim. Cosmochim. Acta* **2006**, *70*, 3625–3645. [CrossRef]
25. Klein, F.; Humphris, S.E.; Guo, W.; Schubotz, F.; Schwarzenbach, E.M.; Orsi, W.D. Fluid mixing and the deep biosphere of a fossil Lost City-type hydrothermal system at the Iberia Margin. *Proc. Natl. Acad. Sci. USA* **2015**, *112*, 12036–12041. [CrossRef] [PubMed]
26. Alt, J.C.; Shanks, W.C. Serpentinization of abyssal peridotites from the MARK area, Mid-Atlantic Ridge: Sulfur geochemistry and reaction modeling. *Geochim. Cosmochim. Acta* **2003**, *67*, 641–653. [CrossRef]
27. Bach, W.; Rosner, M.; Jöns, N.; Rausch, S.; Robinson, L.F.; Paulick, H.; Erzinger, J. Carbonate veins trace seawater circulation during exhumation and uplift of mantle rock: Results from ODP Leg 209. *Earth Planet. Sci. Lett.* **2011**, *311*, 242–252. [CrossRef]
28. Manatschal, G.; Sauter, D.; Karpoff, A.M.; Masini, E.; Mohn, G.; Lagabrielle, Y. The Chenaillet Ophiolite in the French/Italian Alps: An ancient analogue for an oceanic core complex? *Lithos* **2011**, *124*, 169–184. [CrossRef]
29. Schroeder, T.; John, B.E. Strain localization on an oceanic detachment fault system, Atlantis Massif, 30 N.; Mid-Atlantic Ridge. *Geochem. Geophys. Geosyst.* **2004**, *5*. [CrossRef]
30. Bonnemains, D.; Escartín, J.; Mével, C.; Andreani, M.; Verlaguet, A. Pervasive silicification and hanging wall overplating along the 13°20′ N oceanic detachment fault (Mid-Atlantic Ridge). *Geochem. Geophys. Geosyst.* **2017**, *18*, 2028–2053. [CrossRef]
31. Sibson, R.H. Fault rocks and fault mechanisms. *J. Geol. Soc.* **1977**, *133*, 191–213. [CrossRef]
32. Manatschal, G.; Froitzheim, N.; Rubenach, M.; Turrin, B.D. The role of detachment faulting in the formation of an ocean-continent transition: Insights from the Iberia Abyssal Plain: From Wilson, R.L.C.; Whitmarsh, R.B.; Taylor, B.; Froitzheim, N. Non-volcanic rifting of continental margins: A comparaison of evidence from land and sea. *Geol. Soc. Lond. Spec. Publ.* **2001**, *187*, 405–428.
33. Woodcock, N.H.; Mort, K. Classification of fault breccias and related fault rocks. *Geol. Mag.* **2008**, *145*, 435–440. [CrossRef]

34. Agrinier, P.; Mével, C.; Girardeau, J. Hydrothermal alteration of the peridotites cored at the ocean/continent boundary of the Iberian margin: Petrologic and stable isotope evidence. In *Proceedings-Ocean Drilling Program Scientific Results*; Boillot, G., Winterer, E.L., Eds.; National Science Foundation: College Station, TX, USA, 1988; Volume 103, pp. 225–234.
35. Milliken, K.L.; Morgan, J.K. Chemical evidence for near seafloor precipitation of calcite in serpentinites (Site 897) and serpentinite breccias (Site 899), Iberia Abyssal Plain. In *Proceedings of the Ocean Drilling Program, Scientific Results*; Whitmarsh, R.B., Sawyer, D.S., Eds.; National Science Foundation: College Station, TX, USA, 1996; Volume 149.
36. Skelton, A.D.; Valley, J.W. The relative timing of serpentinisation and mantle exhumation at the ocean–continent transition, Iberia: Constraints from oxygen isotopes. *Earth Planet. Sci. Lett.* **2000**, *178*, 327–338. [CrossRef]
37. Whitmarsh, R.B.; Beslier, M.O.; Wallace, P.J. *Proceedings ODP, Initial Reports*; Ocean Drilling Program: College Station, TX, USA, 1998; Volume 173. [CrossRef]
38. Jagoutz, O.; Muntener, O.; Manatschal, G.; Rubatto, D.; Péron-Pinvidic, G.; Turrin, B.D.; Villa, I.M. The rift-to-drift transition in the North Atlantic: A stuttering start of the MORB machine? *Geology* **2007**, *35*, 1087–1090. [CrossRef]
39. Eddy, M.P.; Jagoutz, O.; Ibañez-Mejia, M. Timing of initial seafloor spreading in the Newfoundland-Iberia rift. *Geology* **2017**, *45*, 527–530. [CrossRef]
40. Sutra, E.; Manatschal, G. How does the continental crust thin in a hyperextended rifted margin? Insights from the Iberia margin. *Geology* **2012**, *40*, 139–142. [CrossRef]
41. Machel, H.G.; Mason, R.A.; Mariano, A.N.; Mucci, A. Causes and emission of luminescence in calcite and dolomite. In *Luminescence Microscopy and Spectroscopy—Qualitative and Quantitative Applications. SEPM (Society for Sedimentary Geology) Short Course*; Barker, C.E., Kopp, O.C., Eds.; SEPM: Tulsa, OK, USA, 1991; Volume 25, pp. 9–25.
42. Lane, S.J.; Dalton, J.A. Electron microprobe analysis of geological carbonates. *Am. Mineral.* **1994**, *79*, 745–749.
43. Kim, S.T.; O'Neil, J.R. Equilibrium and nonequilibrium oxygen isotope effects in synthetic carbonates. *Geochim. Cosmochim. Acta* **1997**, *61*, 3461–3475. [CrossRef]
44. Zachos, J.; Pagani, M.; Sloan, L.; Thomas, E.; Billups, K. Trends, rhythms, and aberrations in global climate 65 Ma to present. *Science* **2001**, *292*, 686–693. [CrossRef]
45. Wolery, T.J. *EQ3/6: A Software Package for Geochemical Modeling of Aqueous Systems: Package Overview and Installation Guide (Version 7.0)*; Lawrence Livermore National Laboratory: Livermore, CA, USA, 1992; p. 41.
46. Klein, F.; Bach, W.; Jöns, N.; McCollom, T.; Moskowitz, B.; Berquó, T. Iron partitioning and hydrogen generation during serpentinization of abyssal peridotites from 15° N on the Mid-Atlantic Ridge. *Geochim. Cosmochim. Acta* **2009**, *73*, 6868–6893. [CrossRef]
47. Tutolo, B.M.; Mildner, D.F.; Gagnon, C.V.; Saar, M.O.; Seyfried, W.E., Jr. Nanoscale constraints on porosity generation and fluid flow during serpentinization. *Geology* **2016**, *44*, 103–106. [CrossRef]
48. Johnson, J.W.; Oelkers, E.H.; Helgeson, H.C. SUPCRT92: A software package for calculating the standard molal thermodynamic properties of minerals, gases, aqueous species, and reactions from 1 to 5000 bar and 0 to 1000 C. *Comput. Geosci.* **1992**, *18*, 899–947. [CrossRef]
49. Klein, F.; Bach, W.; McCollom, T.M. Compositional controls on hydrogen generation during serpentinization of ultramafic rocks. *Lithos* **2013**, *178*, 55–69. [CrossRef]
50. Malvoisin, B. Mass transfer in the oceanic lithosphere: Serpentinization is not isochemical. *Earth Planet. Sci. Lett.* **2015**, *430*, 75–85. [CrossRef]
51. Milési, V.; Guyot, F.; Brunet, F.; Richard, L.; Recham, N.; Benedetti, M.; Dairou, J.; Prinzhofer, A. Formation of CO_2, H_2 and condensed carbon from siderite dissolution in the 200–300 °C range and at 50 MPa. *Geochim. Cosmochim. Acta* **2015**, *154*, 201–211. [CrossRef]
52. Evans, B.W. Control of the products of serpentinization by the Fe^{2+} Mg^{-1} exchange potential of olivine and orthopyroxene. *J. Petrol.* **2008**, *49*, 1873–1887. [CrossRef]
53. Andreani, M.; Munoz, M.; Marcaillou, C.; Delacour, A. μXANES study of iron redox state in serpentine during oceanic serpentinization. *Lithos* **2013**, *178*, 70–83. [CrossRef]
54. Emmanuel, S.; Berkowitz, B. Suppression and stimulation of seafloor hydrothermal convection by exothermic mineral hydration. *Earth Planet. Sci. Lett.* **2006**, *243*, 657–668. [CrossRef]
55. Rudge, J.F.; Kelemen, P.B.; Spiegelman, M. A simple model of reaction-induced cracking applied to serpentinization and carbonation of peridotite. *Earth Planet. Sci. Lett.* **2010**, *291*, 215–227. [CrossRef]

56. Malvoisin, B.; Brantut, N.; Kaczmarek, M.A. Control of serpentinisation rate by reaction-induced cracking. *Earth Planet. Sci. Lett.* **2017**, *476*, 143–152. [CrossRef]
57. Lasaga, A.C. *Kinetic Theory in the Earth Sciences*; Princeton University Press: Chichester, UK, 2014; Volume 402.
58. Frost, B.R.; Beard, J.S. On silica activity and serpentinization. *J. Petrol.* **2007**, *48*, 1351–1368. [CrossRef]
59. Saldi, G.D.; Jordan, G.; Schott, J.; Oelkers, E.H. Magnesite growth rates as a function of temperature and saturation state. *Geochim. Cosmochim. Acta* **2009**, *73*, 5646–5657. [CrossRef]
60. Artemyev, D.A.; Zaykov, V.V. The types and genesis of ophicalcites in Lower Devonian olistostromes at cobalt-bearing massive sulfide deposits in the West Magnitogorsk paleoisland arc (South Urals). *Russ. Geol. Geophys.* **2010**, *51*, 750–763. [CrossRef]
61. Boudier, F.; Baronnet, A.; Mainprice, D. Serpentine mineral replacements of natural olivine and their seismic implications: Oceanic lizardite versus subduction-related antigorite. *J. Petrol.* **2010**, *51*, 495–512. [CrossRef]
62. Kelemen, P.B.; Hirth, G. Reaction-driven cracking during retrograde metamorphism: Olivine hydration and carbonation. *Earth Planet. Sci. Lett.* **2012**, *345*, 81–89. [CrossRef]
63. Rouméjon, S.; Cannat, M. Serpentinization of mantle-derived peridotites at mid-ocean ridges: Mesh texture development in the context of tectonic exhumation. *Geochem. Geophys. Geosyst.* **2014**, *15*, 2354–2379. [CrossRef]
64. Rumori, C.; Mellini, M.; Viti, C. Oriented, non-topotactic olivine—Serpentine replacement in mesh-textured, serpentinized peridotites. *Eur. J. Mineral.* **2004**, *16*, 731–741. [CrossRef]
65. Viti, C.; Mellini, M. Mesh textures and bastites in the Elba retrograde serpentinites. *Eur. J. Mineral.* **1998**, *10*, 1341–1359. [CrossRef]
66. Andreani, M.; Grauby, O.; Baronnet, A.; Muñoz, M. Occurrence, composition and growth of polyhedral serpentine. *Eur. J. Mineral.* **2008**, *20*, 159–171. [CrossRef]
67. Müntener, O.; Manatschal, G. High degrees of melt extraction recorded by spinel harzburgite of the Newfoundland margin: The role of inheritance and consequences for the evolution of the southern North Atlantic. *Earth Planet. Sci. Lett.* **2006**, *252*, 437–452. [CrossRef]
68. Klinkhammer, G.; Bender, M.; Weiss, R.F. Hydrothermal manganese in the Galapagos Rift. *Nature* **1977**, *269*, 319–320. [CrossRef]
69. Pingitore, N.E.; Eastman, M.P.; Sandidge, M.; Oden, K.; Freiha, B. The coprecipitation of manganese (II) with calcite: An experimental study. *Mar. Chem.* **1988**, *25*, 107–120. [CrossRef]
70. Haberman, D.; Neuser, R.D.; Richter, D.K. Low limit of Mn^{2+}—Activated cathodoluminescence of calcite: State of the art. *Sediment. Geol.* **1996**, *116*, 13–24. [CrossRef]
71. Dromgoole, E.L.; Walter, L.M. Iron and manganese incorporation into calcite: Effects of growth kinetics, temperature and solution chemistry. *Chem. Geol.* **1990**, *81*, 311–336. [CrossRef]
72. Barnaby, R.J.; Rimstidt, J.D. Redox conditions of calcite cementation interpreted from Mn and Fe contents of authigenic calcites. *Geol. Soc. Am. Bull.* **1989**, *101*, 795–804. [CrossRef]
73. Barnes, I.; O'Neil, J.R. The relationship between fluids in some fresh alpine-type ultramafics and possible modern serpentinization, western United States. *Geol. Soc. Am. Bull.* **1969**, *80*, 1947–1960. [CrossRef]
74. Kitano, Y.; Hood, D.W. Calcium carbonate crystal forms formed from sea water by inorganic processes. *J. Oceanogr. Soc. Jpn.* **1962**, *18*, 35–39. [CrossRef]
75. Müller, G.; Irion, G.; Förstner, U. Formation and diagenesis of inorganic Ca-Mg carbonates in the lacustrine environment. *Naturwissenschaften* **1972**, *59*, 158–164. [CrossRef]
76. Romanek, C.S.; Jiménez-Lopez, C.; Rodriguez Navarro, A.; Sanchez-Roman, M.; Sahai, N.; Coleman, M. Inorganic synthesis of Fe-Ca-Mg carbonates at low temperature. *Geochim. Cosmochim. Acta* **2009**, *73*, 5361–5376. [CrossRef]
77. Martin, B.; Fyfe, W.S. Some experimental and theoretical observations on the kinetics of hydration reactions with particular reference to serpentinization. *Chem. Geol.* **1970**, *6*, 185–202. [CrossRef]
78. Malvoisin, B.; Brunet, F.; Carlut, J.; Rouméjon, S.; Cannat, M. Serpentinization of oceanic peridotites: 2. Kinetics and processes of San Carlos olivine hydrothermal alteration. *J. Geophys. Res. Solid Earth* **2012**, *117*. [CrossRef]
79. Zheng, Y.F. Calculation of oxygen isotope fractionation in hydroxyl-bearing silicates. *Earth Planet. Sci. Lett.* **1993**, *120*, 247–263. [CrossRef]
80. Wenner, D.B.; Taylor, H.P. Temperatures of serpentinization of ultramafic rocks based on O^{18}/O^{16} fractionation between coexisting serpentine and magnetite. *Contrib. Mineral. Petrol.* **1971**, *32*, 165–185. [CrossRef]

81. Baumgartner, L.P.; Valley, J.W. Stable isotope transport and contact metamorphic fluid flow. *Rev. Mineral. Geochem.* **2001**, *43*, 415–467. [CrossRef]
82. Boschi, C.; Dini, A.; Baneschi, I.; Bedini, F.; Perchiazzi, N.; Cavallo, A. Brucite-driven CO_2 uptake in serpentinized dunites (Ligurian Ophiolites, Montecastelli, Tuscany). *Lithos* **2017**, *288*, 264–281. [CrossRef]
83. Kelemen, P.B.; Matter, J.; Streit, E.E.; Rudge, J.F.; Curry, W.B.; Blusztajn, J. Rates and mechanisms of mineral carbonation in peridotite: Natural processes and recipes for enhanced, in situ CO_2 capture and storage. *Annu. Rev. Earth Planet. Sci.* **2011**, *39*, 545–576. [CrossRef]
84. Früh-Green, G.L.; Weissert, H.; Bernoulli, D. A multiple fluid history recorded in Alpine ophiolites. *J. Geol. Soc.* **1990**, *147*, 959–970. [CrossRef]
85. Pozzorini, D.; Früh-Green, G.L. Stable isotope systematics of the Ventina Ophicarbonate Zone, Bergell contact aureole. *Schweiz. Mineral. und Petrol. Mitt.* **1996**, *76*, 549–564.
86. Abart, R.; Pozzorini, D. Implications of kinetically controlled mineral-fluid exchange on the geometry of stable-isotope fronts. *Eur. J. Miner.* **2000**, *12*, 1069–1082. [CrossRef]
87. Manatschal, G.; Nievergelt, P. A continent-ocean transition recorded in the Err and Platta nappes (Eastern Switzerland). *Eclogae Geol. Helv.* **1997**, *90*, 3–28.
88. Driesner, T. Aspects of petrographical, structural and stable isotope geochemical evolution of ophicarbonates breccias from ocean floor to subduction and uplift: An example from Chatillon, Middle Aosta Valley, Italian Alps. *Schweiz. Mineral. und Petrol. Mitt.* **1993**, *73*, 69–84.
89. Farver, J.R. Oxygen self-diffusion in calcite: Dependence on temperature and water fugacity. *Earth Planet. Sci. Lett.* **1994**, *121*, 575–587. [CrossRef]
90. Labotka, T.C.; Cole, D.R.; Riciputi, L.R. Diffusion of C and O in calcite at 100 MPa. *Am. Mineral.* **2000**, *85*, 488–494. [CrossRef]
91. Rosenbaum, J.M. Stable isotope fractionation between carbon dioxide and calcite at 900 °C. *Geochim. Cosmochim. Acta* **1994**, *58*, 3747–3753. [CrossRef]
92. Benson, S.M.; Cole, D.R. CO_2 sequestration in deep sedimentary formations. *Elements* **2008**, *4*, 325–331. [CrossRef]
93. Xu, T.; Apps, J.A.; Pruess, K. Numerical simulation of CO_2 disposal by mineral trapping in deep aquifers. *Appl. Geochem.* **2004**, *19*, 917–936. [CrossRef]
94. Andreani, M.; Luquot, L.; Gouze, P.; Godard, M.; Hoise, E.; Gibert, B. Experimental study of carbon sequestration reactions controlled by the percolation of CO_2-rich brine through peridotites. *Environ. Sci. Technol.* **2009**, *43*, 1226–1231. [CrossRef]
95. Boschi, C.; Dini, A.; Dallai, L.; Ruggieri, G.; Gianelli, G. Enhanced CO_2-mineral sequestration by cyclic hydraulic fracturing and Si-rich fluid infiltration into serpentinites at Malentrata (Tuscany, Italy). *Chem. Geol.* **2009**, *265*, 209–226. [CrossRef]
96. King, H.E.; Plümper, O.; Putnis, A. Effect of secondary phase formation on the carbonation of olivine. *Environ. Sci. Technol.* **2010**, *44*, 6503–6509. [CrossRef]
97. Paukert, A.N.; Matter, J.M.; Kelemen, P.B.; Shock, E.L.; Havig, J.R. Reaction path modeling of enhanced in situ CO_2 mineralization for carbon sequestration in the peridotite of the Samail Ophiolite, Sultanate of Oman. *Chem. Geol.* **2012**, *330*, 86–100. [CrossRef]
98. Klein, F.; McCollom, T.M. From serpentinization to carbonation: New insights from a CO_2 injection experiment. *Earth Planet. Sci. Lett.* **2013**, *379*, 137–145. [CrossRef]
99. Power, I.M.; Wilson, S.A.; Dipple, G.M. Serpentinite carbonation for CO_2 sequestration. *Elements* **2013**, *9*, 115–121. [CrossRef]